

# Far-infrared line emission from the outer Galaxy cluster Gy 3–7 with SOFIA/FIFI-LS: Physical conditions and UV fields<sup>★</sup>

Ngân Lê<sup>1</sup>, A. Karska<sup>1,2\*\*</sup>, M. Figueira<sup>3,1</sup>, M. Sewiło<sup>4,5,6</sup>, A. Mirocha<sup>7</sup>, Ch. Fischer<sup>8</sup>, M. Kaźmierczak-Barthel<sup>8</sup>, R. Klein<sup>9</sup>, M. Gawroński<sup>1</sup>, M. Koprowski<sup>1</sup>, K. Kowalczyk<sup>1</sup>, W. J. Fischer<sup>10</sup>, K. M. Menten<sup>2</sup>, F. Wyrowski<sup>2</sup>, C. König<sup>2</sup>, L. E. Kristensen<sup>11</sup>

<sup>1</sup> Institute of Astronomy, Faculty of Physics, Astronomy and Informatics, Nicolaus Copernicus University, Grudziądzka 5, 87-100 Toruń, Poland

<sup>2</sup> Max-Planck-Institut für Radioastronomie, Auf dem Hügel 69, 53121, Bonn, Germany

<sup>3</sup> National Centre for Nuclear Research, ul. Pasteura 7, 02-093, Warszawa, Poland

<sup>4</sup> Exoplanets and Stellar Astrophysics Laboratory, NASA Goddard Space Flight Center, Greenbelt, MD 20771, USA

<sup>5</sup> Center for Research and Exploration in Space Science and Technology, NASA Goddard Space Flight Center, Greenbelt, MD 20771

<sup>6</sup> Department of Astronomy, University of Maryland, College Park, MD 20742, USA

<sup>7</sup> Astronomical Observatory of the Jagiellonian University, Orla 171, 30-244, Kraków, Poland

<sup>8</sup> Deutsches SOFIA Institut, University of Stuttgart, Pfaffenwaldring 29, 70569, Stuttgart

<sup>9</sup> SOFIA/USRA, NASA Ames Research Center, P.O. Box 1, MS 232-12, Moffett Field, CA 94035, USA

<sup>10</sup> Space Telescope Science Institute, 3700 San Martin Dr., Baltimore, MD 21218, USA

<sup>11</sup> Niels Bohr Institute, Centre for Star and Planet Formation, University of Copenhagen, Øster Voldgade 5-7, 1350 Copenhagen, Denmark

Received February 14, 2023; accepted April 10, 2023

## ABSTRACT

**Context.** Far-infrared (FIR) line emission provides key information about the gas cooling and heating due to shocks and UV radiation associated with the early stages of star formation. Gas cooling via FIR lines might, however, depend on metallicity.

**Aims.** We aim to quantify the FIR line emission and determine the spatial distribution of the CO rotational temperature, ultraviolet (UV) radiation field, and H<sub>2</sub> number density toward the embedded cluster Gy 3–7 in the CMA–I224 star-forming region, whose metallicity is expected to be intermediate between that of the Large Magellanic Cloud and the Solar neighborhood. By comparing the total luminosities of CO and [O I] toward Gy 3–7 with values found for low- and high-mass protostars extending over a broad range of metallicities, we also aim to identify the possible effects of metallicity on the FIR line cooling within our Galaxy.

**Methods.** We studied SOFIA/FIFI-LS spectra of Gy 3–7, covering several CO transitions from  $J = 14 - 13$  to  $31 - 30$ , the OH doublet at  $79 \mu\text{m}$ , the [O I]  $63.2$  and  $145.5 \mu\text{m}$ , and the [C II]  $158 \mu\text{m}$  lines. The field of view covers a  $2' \times 1'$  region with a resolution of  $\sim 7'' - 18''$ .

**Results.** The spatial extent of CO high- $J$  ( $J_{\text{up}} \geq 14$ ) emission resembles that of the elongated  $160 \mu\text{m}$  continuum emission detected with *Herschel*, but its peaks are offset from the positions of the dense cores. The [O I] lines at  $63.2 \mu\text{m}$  and  $145.5 \mu\text{m}$  follow a similar pattern, but their peaks are found closer to the positions of the cores. The CO transitions from  $J = 14 - 13$  to  $J = 16 - 15$  are detected throughout the cluster and show a median rotational temperature of  $170 \pm 30$  K on Boltzmann diagrams. Comparisons to other protostars observed with *Herschel* show a good agreement with intermediate-mass sources in the inner Galaxy. Assuming an origin of the [O I] and high- $J$  CO emission in UV-irradiated C-shocks, we obtained pre-shock H<sub>2</sub> number densities of  $10^4 - 10^5 \text{ cm}^{-3}$  and UV radiation field strengths of 0.1–10 Habing fields ( $G_0$ ).

**Conclusions.** Far-IR line observations reveal ongoing star formation in Gy 3–7, dominated by intermediate-mass Class 0/I young stellar objects. The ratio of molecular-to-atomic far-IR line emission shows a decreasing trend with bolometric luminosities of the protostars. However, it does not indicate that the low-metallicity has an impact on the line cooling in Gy 3–7.

**Key words.** stars:formation – stars: protostars – ISM: jets and outflows – ISM: molecules

## 1. Introduction

During the earliest stages of star formation, the gravitational collapse of dense cores is accompanied by an ejection of bipolar jets originating from the resulting protostars, which may al-

ter the physical conditions and chemistry of their environment, even on clump scales (Arce et al. 2007; Frank et al. 2014). Non-dissociative shock waves develop as the jets (and winds) interact with the surrounding medium (Kaufman & Neufeld 1996a; Flower & Pineau des Forêts 2012) and heat up the gas up to typically  $\sim 300$  K (Karska et al. 2018; Yang et al. 2018). Additionally, ultraviolet (UV) photons contribute to the gas heating and influence the chemical composition of the low- to high-mass protostars' envelopes (Bruderer et al. 2009; Visser et al. 2012). Similarly to some pc-scale outflows, UV photons may operate over a significant fraction of low-mass star-forming clumps and

<sup>★</sup> Tables 2, 4, A.1, B.1, C.1, D.1, and D.2 are available in electronic form at the CDS via anonymous ftp to [cdsarc.cds.unistra.fr](https://cdsarc.cds.unistra.fr) (130.79.128.5) or via <https://cdsarc.cds.unistra.fr/cgi-bin/qcat?J/A+A/>

<sup>\*\*</sup> Corresponding author: Agata Karska  
e-mail: [agata.karska@umk.pl](mailto:agata.karska@umk.pl)

clusters (Mirocha et al. 2021). The cooling of the gas, which in the case of embedded objects is dominated by line emission in the far-infrared (FIR) and (sub)millimeter domains, provides important constraints on the heating mechanisms and observations of these cooling lines allow us to constrain gas temperatures, densities, and UV fields (Goldsmith & Langer 1978; Hollenbach & McKee 1989).

Recent observations with the *Herschel* Space Observatory (Pilbratt et al. 2010)<sup>1</sup> targeted the main gas cooling lines toward a significant sample of protostars spanning a broad range of masses (van Dishoeck et al. 2021). In particular, the Photodetector Array Camera and Spectrometer (PACS; Poglitsch et al. 2010) provided detections of high- $J$  CO ( $J_{\text{up}} \geq 14$ ), H<sub>2</sub>O, and OH lines, as well as forbidden transitions of [O I] and [C II], all of them being important diagnostic tools in molecular clouds. Among the key findings with PACS are the following: (i) the presence of ubiquitous "warm" gas ( $\sim 300$  K) associated with low- to high-mass protostars (Green et al. 2013; Manoj et al. 2013; Karska et al. 2013, 2014a; Matuszak et al. 2015); (ii) the detection of a plethora of high- $J$  CO (up to 49 – 48;  $E_{\text{u}} \sim 6700$  K) and H<sub>2</sub>O (up to  $E_{\text{u}} \sim 1500$  K) lines tracing the "hot" gas component (Herczeg et al. 2012; Goicoechea et al. 2012), with a median temperature of  $\sim 720$  K (Karska et al. 2018); (iii) the identification of the origin of the FIR line emission in UV-irradiated non-dissociative shocks extending along the outflows (Karska et al. 2014b; Benz et al. 2016; Kristensen et al. 2017b; Karska et al. 2018); and (iv) the recognition of the dominant role of CO and H<sub>2</sub>O in the gas cooling budget of low-mass (LM) protostars (Karska et al. 2013, 2018) as well as CO and [O I] as coolants of high-mass (HM) protostars (Karska et al. 2014a). The above observations have provided a surprisingly uniform picture of the FIR line emission from deeply-embedded protostars, but targeted only on relatively nearby regions ( $d < 450$  pc in case of LM objects van Dishoeck et al. 2021).

Observations of the Large and Small Magellanic Clouds (LMC and SMC) with *Herschel* have shed some light on the FIR line cooling from protostars in a significantly different, low-metallicity environment ( $Z$  of 0.2–0.5  $Z_{\odot}$ ; Russell & Dopita 1992). The Spectral and Photometric Imaging Receiver (SPIRE, Griffin et al. 2010) and PACS provided detections of CO (up to  $J=14-13$ ), H<sub>2</sub>O, OH, and [O I], and [C II] lines, facilitating comparisons with Galactic sources (Oliveira et al. 2019). The CO emission toward 15 sources in the LMC showed two relatively cool gas components, with temperatures of  $\sim 40$  and  $\sim 120$  K, consistent with Galactic measurements using SPIRE (White et al. 2010; Jiménez-Donaire et al. 2017; Yang et al. 2018). The line cooling budget of protostars in the Magellanic Clouds is dominated by [O I] and [C II] emission, with an increasing contribution of CO as the metallicity increases from the SMC to LMC and to the Galactic young stellar objects (YSOs, Karska et al. 2014a; Oliveira et al. 2019). The low fraction of CO line cooling is interpreted as a metallicity effect: the combined result of a reduced carbon abundance and higher grain temperatures due to a lower shielding from UV photons (Oliveira et al. 2019).

The outer parts of our Galaxy provide an alternative site for testing the impact of metallicity on the FIR gas properties of protostars. Due to the negative-metallicity gradient, the abundances of dust and molecules decrease in the outer Galaxy (Sodroski et al. 1997). The metallicity affects the gas and dust cooling budget of molecular clouds and results in lower CO rotational tem-

peratures,  $T_{\text{rot}}$  (Roman-Duval et al. 2010). Despite the overall decreasing trend of the mass surface density of molecular clouds in the outer Galaxy (for a review, see Heyer & Dame 2015), some star-forming regions show a significant star-formation activity. For example, the CMA-1224 star-forming region at a Galactocentric radius,  $R_{\text{GC}}$ , of 9.1 kpc consists of  $\sim 290$  Class I/II YSOs, as identified by Sewilo et al. (2019) using data from GLIMPSE360: Completing the Spitzer Galactic Plane Survey (PI: B. Whitney) and the Herschel infrared Galactic Plane Survey (Hi-GAL; Molinari et al. 2010, see also Elia et al. 2013). The expected metallicity of this region is  $\sim 0.55-0.73 Z_{\odot}$ , depending on the adopted O/H Galactocentric radial gradient (Balsler et al. 2011; Fernández-Martín et al. 2017; Esteban & García-Rojas 2018).

Gy 3–7 is a deeply-embedded cluster with exceptionally bright FIR continuum emission, located at the second-most massive filament in the CMA-1224 region (Sewilo et al. 2019) at a distance of  $\sim 1$  kpc (e.g., Lombardi et al. 2011). It is associated with IRAS 07069–1045, which was recognized early on as a star-forming region driving a CO outflow, with a bolometric luminosity ( $L_{\text{bol}}$ ) of  $980 L_{\odot}$  (assuming a distance of 1.4 kpc; Wouterloot & Brand 1989). The source was considered as a candidate HM star-forming region based on its position in the IRAS color-color diagrams and the presence of dense gas traced by CS 2 – 1 (Wood & Churchwell 1989; Bronfman et al. 1996). However, several attempts have failed to detect the CH<sub>3</sub>OH maser emission, which is a common signature of HM protostars (Menten et al. 1992; Szymczak et al. 2000). Instead, H<sub>2</sub>O maser and thermal NH<sub>3</sub> emission was detected as part of the Red MSX Survey (RMS; Urquhart et al. 2011, see Figure 1).

Recent FIR observations with *Herschel*/Hi-GAL spatially resolved two dense cores in Gy 3–7 with  $L_{\text{bol}}$  of 75.9 and 324.2  $L_{\odot}$ , the latter corresponding to IRAS 07069–1045 (Elia et al. 2013, 2021, see Figure 1). Near-IR observations revealed an extended H<sub>2</sub> emission, which may arise from the jets from protostars (Navarete et al. 2015). Gy 3–7 contains several more evolved YSOs, with spectral types ranging from B1 to B5 (Gyulbudaghian 2012; Tapia et al. 1997) and it is cataloged as a young stellar cluster (Soares & Bica 2002, 2003; Bica et al. 2003).

In this paper, we investigate the FIR line emission toward Gy 3–7 obtained using the Stratospheric Observatory for Infrared Astronomy (SOFIA) observations with the Field-Imaging Far-Infrared Line Spectrometer (FIFI-LS; Klein et al. 2014; Fischer et al. 2018). We also consider the gas densities and UV radiation fields in Gy 3–7, as well as the stellar content of the cluster. We examine whether the rotational temperatures and the ratio of CO and [O I] line luminosities in Gy 3–7 are consistent with the picture of star formation in the inner Galaxy and/or the low-metallicity environment of the Magellanic Clouds. Finally, we also present the results of our search for water masers with the Toruń 32-m radio telescope (RT4).

The paper is organized as follows. Section 2 describes the observations with SOFIA and RT4. In Section 3, we present line and continuum maps, as well as the line profiles at selected positions of interest. Section 4 shows the analysis of the results and Section 5 provides the discussion of the results in the context of previous studies. We provide our summary and conclusions in Section 6.

## 2. Observations

### 2.1. SOFIA FIFI-LS

SOFIA/FIFI-LS observations were collected in November 2019 as part of the SOFIA Cycle 7 (Project ID 07\_0157, PI: M.

<sup>1</sup> *Herschel* was an ESA space observatory with science instruments provided by European-led Principal Investigator consortia and with important participation from NASA.

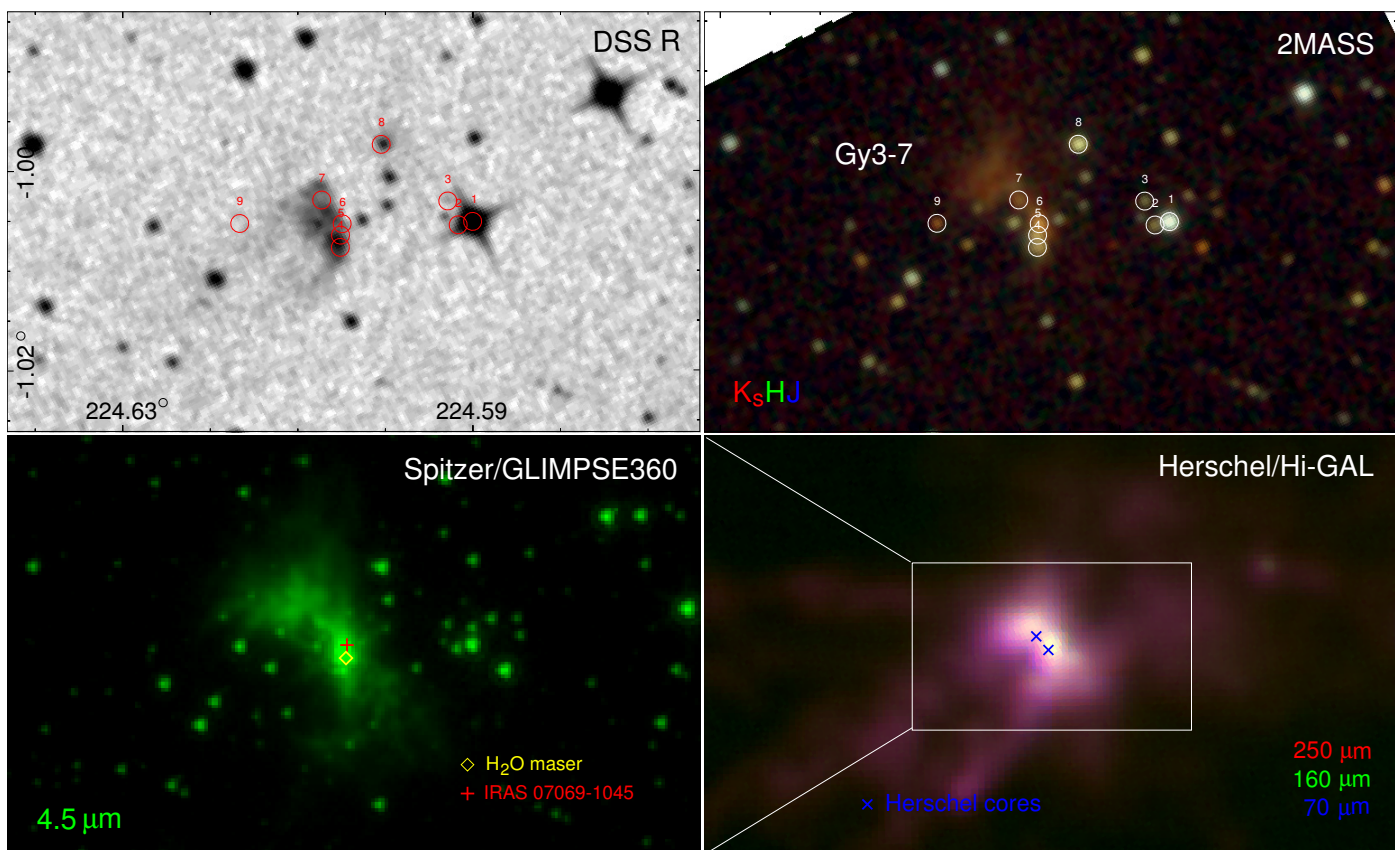


Fig. 1: Digital Sky Survey (DSS) R (top left), 2MASS composite image using the J, H, and  $K_s$  filters (top right), *Spitzer*/GLIMPSE360 4.5  $\mu\text{m}$  (Sewilo et al. 2019; bottom left), and *Herschel*/Hi-GAL composite image at 70, 160, and 250  $\mu\text{m}$  (Elia et al. 2013; bottom right) of the Gy 3–7 cluster. Circles in the top panels show the positions of YSO candidates from Tapia et al. (1997). Yellow diamond and red cross in the bottom-left panel show the position of the  $\text{H}_2\text{O}$  maser (Urquhart et al. 2011) and the IRAS source at the south-west side (IRAS 07069–1045), respectively. The blue “x” symbols in the bottom right panel show the positions of dense cores as traced by the  $\text{H}_2$  column density (Elia et al. 2013). Dense core in the west corresponds to IRAS 07069–1045.

Kaźmierczak-Barthel). FIFI-LS is an integral field unit consisting of two grating spectrometers with a spectral coverage ranging from 51 to 120  $\mu\text{m}$  (blue) and from 115 to 200  $\mu\text{m}$  (red), facilitating simultaneous observations of selected wavelength intervals (0.3–0.9  $\mu\text{m}$ ) in both channels (SOFIA Observer’s Handbook for Cycle 10<sup>2</sup>). The spectral resolution,  $R$ , ranges from  $\sim 500$  to 2000 and increases with wavelength for a given grating order. The corresponding velocity resolution of  $\sim 150$  to 600  $\text{km s}^{-1}$  provides unresolved spectral profiles of all the FIR lines, including  $\text{H}_2\text{O}$  (Kristensen et al. 2012; Mottram et al. 2017), CO (Kristensen et al. 2017b), and [O I] (Kristensen et al. 2017a; Yang et al. 2022a).

The FIFI-LS detector is composed of  $5 \times 5$  spatial pixels (hereafter *spaxels*) with the centers offset by  $10''$ , similar to the PACS spectrometer on *Herschel*. The spaxel size is  $6'' \times 6''$  in the blue channel (field of view, FOV, of  $30'' \times 30''$ ) and  $12'' \times 12''$  in the red channel (FOV of  $1' \times 1'$ ), providing an improvement over PACS by matching the actual wavelength-dependent beam sizes. The FIR sky background was subtracted by symmetric chopping around the telescope’s optical axis with a matched telescope nod. The 300'' throw in the east-west direction was chosen to avoid contaminated regions.

<sup>2</sup> <https://www-sofia.atlassian.net/wiki/spaces/OHFC1/overview>

Table 1 shows the full catalog of lines targeted with FIFI-LS. The maps of the [O I] line at 63.2  $\mu\text{m}$  and the [C II] line at 157.7  $\mu\text{m}$  were obtained simultaneously as  $2 \times 2$  mosaics, with a FOV of  $60'' \times 60''$  in the blue channel and  $90'' \times 90''$  in the red channel, during the wall-clock time of 51 minutes. The maps of the remaining lines were collected as a single FOV with dithering. The total observing time was 239 minutes ( $\sim 4$  hours).

The data were reduced with the SOFIA FIFI-LS pipeline (Vacca et al. 2020), which contains all the necessary calibrations and flat-field corrections. For the telluric correction in the pipeline reduction, we used water vapor values obtained with the method described in Fischer et al. (2021) and Iserlohe et al. (2021). Then, the IDL-based software FLUXER v.2.78<sup>3</sup> was used to produce the continuum and line emission maps. The continuum was fitted as a 0th order polynomial in spectral areas free of line emission and the spectral line was fitted with a Gaussian. The selection of channels for the baseline subtraction, the observed wavelength of the targeted line and its width were obtained over the area with strong line detections, separately for each species. Subsequently, these values were adopted for the entire datacube to obtain the integrated line fluxes for the entire map. Further processing of the maps was performed with Python.

<sup>3</sup> <http://ciserlohe.de/fluxer/fluxer.html>



Table 1: Catalog of lines observed with FIFI-LS toward Gy 3–7

Line	Transition	$E_u/k_B$ (K)	$A_u$ ( $s^{-1}$ )	$g_u$	$\lambda_{lab}$ ( $\mu m$ )	Map size ("×")	Beam (")
CO	14 – 13	580.5	2.7(-4)	29	185.99	60×60	18.3
CO	16 – 15	751.7	4.1(-4)	33	162.81	60×60	16.1
CO	17 – 16	845.6	4.8(-4)	35	153.27	60×60	15.2
CO	22 – 21	1397.4	1.0(-3)	45	118.58	30×30	11.9
CO	30 – 29	2564.9	2.3(-3)	61	87.19	30×30	8.6
CO <sup>a</sup>	31-30	2735.3	2.5(-3)	63	84.41	30×30	8.3
OH <sup>b</sup>	$\frac{1}{2}, \frac{1}{2} - \frac{3}{2}, \frac{1}{2}$	270.1	6.5(-2)	4	163.12	60×60	16.1
OH <sup>c</sup>	$\frac{1}{2}, \frac{1}{2} - \frac{3}{2}, \frac{3}{2}$	181.7	2.9(-2)	3	79.18	30×30	7.9
OH <sup>a</sup>	$\frac{7}{2}, \frac{3}{2} - \frac{5}{2}, \frac{3}{2}$	290.5	5.1(-1)	9	84.42	30×30	8.3
[O I]	$^3P_0 - ^3P_2$	227.7	8.9(-5)	3	63.18	60×60	7.1
[O I]	$^3P_1 - ^3P_2$	326.6	1.8(-5)	1	145.52	60×60	14.4
[C II]	$^2P_{3/2} - ^2P_{1/2}$	91.2	2.4(-6)	5	157.74	90×90	15.6

**Notes.** Molecular data adopted from the Leiden Atomic and Molecular Database (LAMDA, Schöier et al. 2005) and the JPL database (Pickett et al. 1998). <sup>(a)</sup> CO 31-30 and OH line at 84.42  $\mu m$  are blended. <sup>(b)</sup> OH line at 163.12  $\mu m$  is not detected. <sup>(c)</sup> The 79.18  $\mu m$  is detected at the band edge, and its line fluxes cannot be securely measured due to the lack of a baseline.

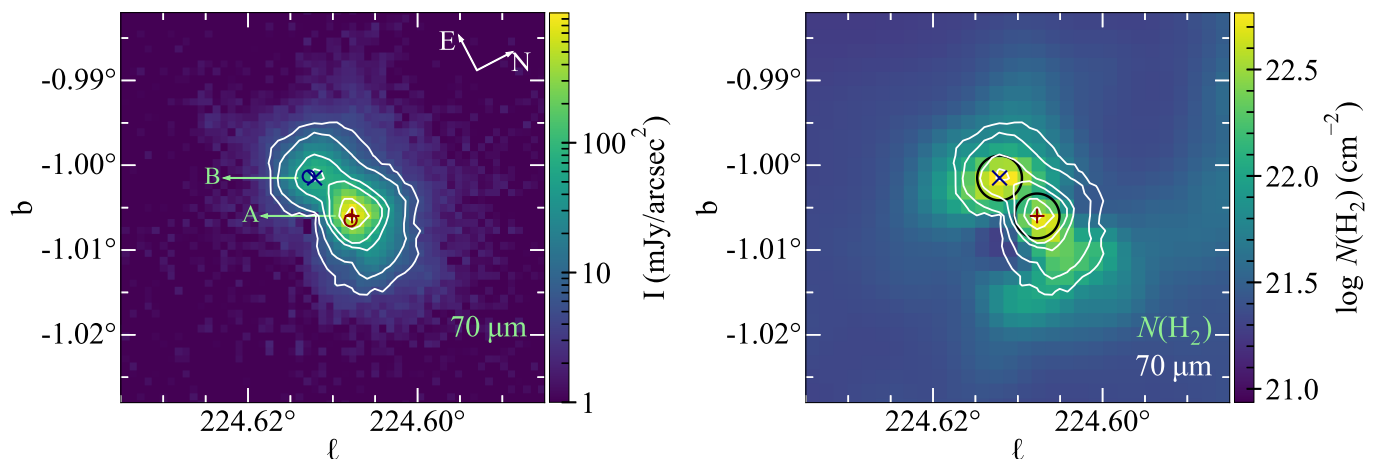


Fig. 2: Distribution of dust continuum emission toward Gy 3–7. Left: Continuum map of Gy 3–7 at 70  $\mu m$  observed with *Herschel*/PACS. Red “+” and blue “×” symbols refer to the 70  $\mu m$  continuum peaks, adopted as the positions for the dense cores A and B in the subsequent analysis. Circles show the positions of HIGALBM224.6079–1.0065 and HIGALBM224.6128–1.0013 cores from the *Herschel*/Hi-GAL catalog (Elia et al. 2021). Right: Map of the  $H_2$  column density ( $N(H_2)$ ). Black circles with the beam size of 20'' indicate the extract regions of the SOFIA FIFI-LS spectra toward the two dense cores A and B (see more in Section 3.1). White contours in each map show the continuum at 70  $\mu m$ , with contour levels at 5, 10, 40, 80, 400, and 800 mJy/arcsec<sup>2</sup>.

The overall calibration accuracy can be assumed to be within 20%, including a 10% calibration accuracy of the instrument, and the additional uncertainty due to telluric effect, which is assumed to be well under 10%. For the [O I] line at 63.2  $\mu m$ , located close to the water absorption line, the water vapor overburden was determined between 3.5 and 3.7  $\mu m$ . With an error of 10% on this water vapor range, this results in a transmission at the line location of 78-83%.

## 2.2. *Herschel*/PACS

We used the *Herschel*/PACS 70  $\mu m$  continuum map to verify the positions of the dense cores in Gy 3–7 listed in

the *Herschel*/Hi-GAL compact source catalogue<sup>4</sup> (Elia et al. 2021). Figure 2 shows the 70  $\mu m$  continuum map and the  $H_2$  column density,  $N(H_2)$ , map obtained using the *ppmap* tool with the *Herschel*/Hi-GAL survey (Marsh et al. 2017). Overall, there is a good agreement between the catalog positions and the peaks in the continuum at 70  $\mu m$  and  $N(H_2)$ . In the subsequent analysis, we adopt the coordinates of the 70  $\mu m$  peaks as the dense core coordinates. We refer to the core at (RA, Dec) = (7<sup>h</sup>09<sup>m</sup>20<sup>s</sup>.4, –10°50′28″.4) as A and to that at (7<sup>h</sup>09<sup>m</sup>21<sup>s</sup>.9, –10°50′35″) as B; they correspond to the *Herschel*/Hi-GAL catalog sources HIGALBM224.6079–1.0065 and HIGALBM224.6128–1.0013, respectively (Elia et al. 2021).

<sup>4</sup> [https://vialactea.iaps.inaf.it/vialactea/public/HiGAL\\_360\\_clump\\_catalogue.tar.gz](https://vialactea.iaps.inaf.it/vialactea/public/HiGAL_360_clump_catalogue.tar.gz)

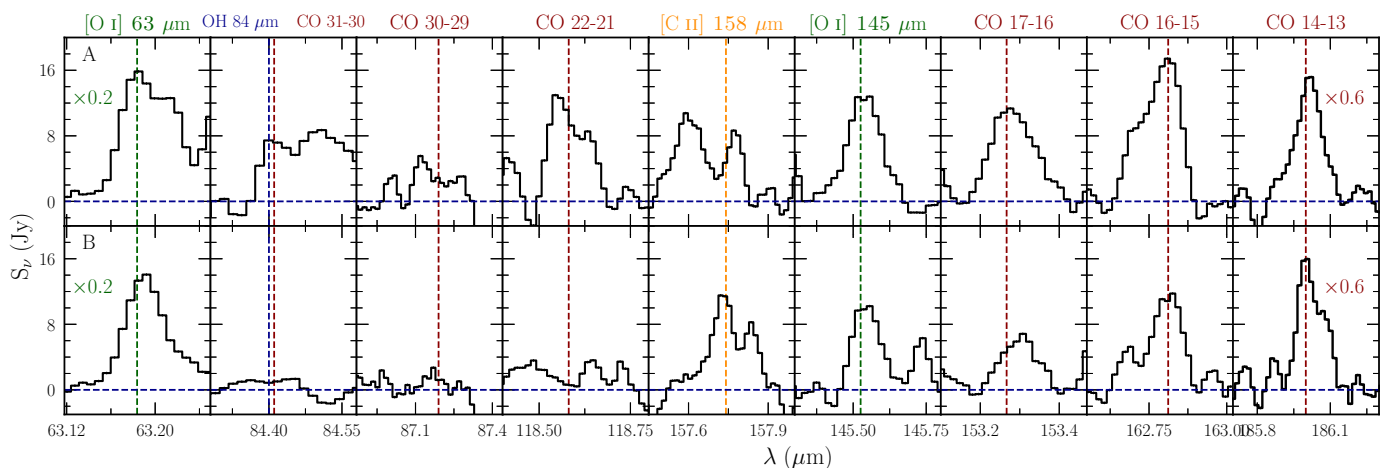


Fig. 3: SOFIA FIFI-LS continuum-subtracted spectra toward the two dense cores in Gy 3–7: HIGALBM224.6079–1.0065 (source “A”) and HIGALBM224.6128–1.0013 (source “B”). The emission is extracted within a beam size of  $20''$  indicated by black circles in the right panel of Figure 2. Vertical lines show the laboratory wavelengths of the detected lines. Spectra of the [O I] line at  $63 \mu\text{m}$  are multiplied by a factor of 0.2 and those of the CO 14 – 13 line by a factor of 0.6 to better illustrate the line detections.

### 2.3. RT4

We conducted a survey at 22 GHz using the Toruń 32-m radio telescope (RT4) toward the entire CMA–1224 region. The full-beam width at half maximum of the antenna at 22 GHz is  $\sim 106''$ , with a pointing error of  $\lesssim 12''$  (Lew 2018).

Two series of observations were performed from 2019 April to 2020 January and from 2020 January to May 2020 in which a total of 205 positions were observed. We used the correlator with  $2 \times 4096$  channels and 8 MHz bandwidth operating in the frequency-switching mode, which provided a local standard of rest velocity coverage from  $-11.9$  to  $41.9 \text{ km s}^{-1}$ . The spectral resolution of the observations is  $0.03 \text{ km s}^{-1}$ . The observations were calibrated by the chopper wheel method and corrected for the gain elevation effect. The system temperature varied from  $\sim 120 \text{ K}$  during winter to  $\sim 200 \text{ K}$  in summer. Overall, the  $3\sigma$  detection limit was between  $\sim 3.8$  and  $\sim 7.5 \text{ Jy}$  per  $0.03 \text{ km s}^{-1}$  channel. The telescope pointing was checked every  $\sim 2$  hrs by observing a nearby bright, point source. We successfully detected a variable water maser emission at (RA, Dec) = ( $7^{\text{h}}09^{\text{m}}21^{\text{s}}.05$ ,  $-10^{\circ}50'05''.4$ ), in direct vicinity of Gy 3–7, and at (RA, Dec) = ( $7^{\text{h}}09^{\text{m}}22^{\text{s}}.66$ ,  $-10^{\circ}30'45''.6$ ), associated with IRAS 07069–1026 (see Appendix A).

## 3. Results

Near-IR images of Gy 3–7 reveal an extended nebulosity associated with the two Hi-GAL dense cores and several YSO candidates (see Figure 1). Spatially-resolved FIR line emission data obtained with FIFI-LS allows us to study key gas cooling lines at  $\sim 10\,000$  au scales and identify regions where processes responsible for the gas heating are at play.

### 3.1. Line detections

Figure 3 shows the FIR line emission toward the two Hi-GAL dense cores in Gy 3–7 (see Section 2.2; for the full list of targeted lines see Table 1). All lines are spectrally-unresolved with FIFI-LS and can be represented by single Gaussian profiles (Section 2.1).

The spectra show strong line emission in the [O I] lines at  $63 \mu\text{m}$  and  $145 \mu\text{m}$ , as well as in the high- $J$  CO lines: the CO 14 – 13 line at  $186.0 \mu\text{m}$ , the CO 16 – 15 line at  $162.8 \mu\text{m}$ , and the CO 17 – 16 line at  $152.3 \mu\text{m}$ . Core A shows also a detection of the CO 22 – 21 line at  $118.6 \mu\text{m}$  ( $E_{\text{u}}$  of  $\sim 1400 \text{ K}$ ) and a tentative detection of CO 30 – 29 line at  $87.2 \mu\text{m}$  ( $E_{\text{u}}$  of  $\sim 2600 \text{ K}$ ). The CO 31 – 30 line at  $84.41 \mu\text{m}$  is blended with the OH line at  $84.42 \mu\text{m}$ , and due to the lack of baseline covering the OH  $84.6 \mu\text{m}$  line from the doublet, its emission cannot be quantified. The OH doublet at  $\sim 79.2 \mu\text{m}$  seems to be tentatively detected toward both cores, but is severely affected by the rise of the baseline on its left side and its flux cannot be properly measured (Appendix B). The OH doublet at  $163.12$  and  $163.18 \mu\text{m}$ , located next to the CO 16–15 line, is not detected in neither of the two cores.

The [O I] line at  $63.18 \mu\text{m}$  sits on the edge of a telluric water feature and the low transmission at  $\lambda \gtrsim 63.24 \mu\text{m}$  increases the noise on the continuum. Since the transmission at the spectral line location is well known and the S/N is very high, there is no relevant effect on the uncertainty of the line flux. Possible self-absorption of this [O I] line cannot be identified at the spectral resolution of FIFI-LS. The higher-resolution spectra collected toward other YSOs using the German REceiver for Astronomy at Terahertz Frequencies (GREAT; Risacher et al. 2018) show that self-absorption could decrease the integrated emission of the line by a factor of 2–3 (Leurini et al. 2015; Mookerjee et al. 2021).

Similarly, self-absorption in the [C II] line at  $157.7 \mu\text{m}$  might affect the FIFI-LS spectra. Strong self-absorption unresolved by FIFI-LS may result in a non-detection of this line toward core A. In contrast, the line is clearly detected toward core-B. Decreases of the flux of [C II] line due to self-absorption as high as a factor of 20 have been estimated toward photodissociation regions (Guevara et al. 2020).

In summary, FIFI-LS spectra provide detections of key FIR cooling lines toward two dense cores in Gy 3–7: the high- $J$  CO, [O I], and [C II]. Due to the atmospheric absorption, the  $\text{H}_2\text{O}$  emission could not be targeted; the OH emission suffers from line blending and poor baselines. In Section 3.2, we show the distribution of line emission in various species toward the entire cluster.

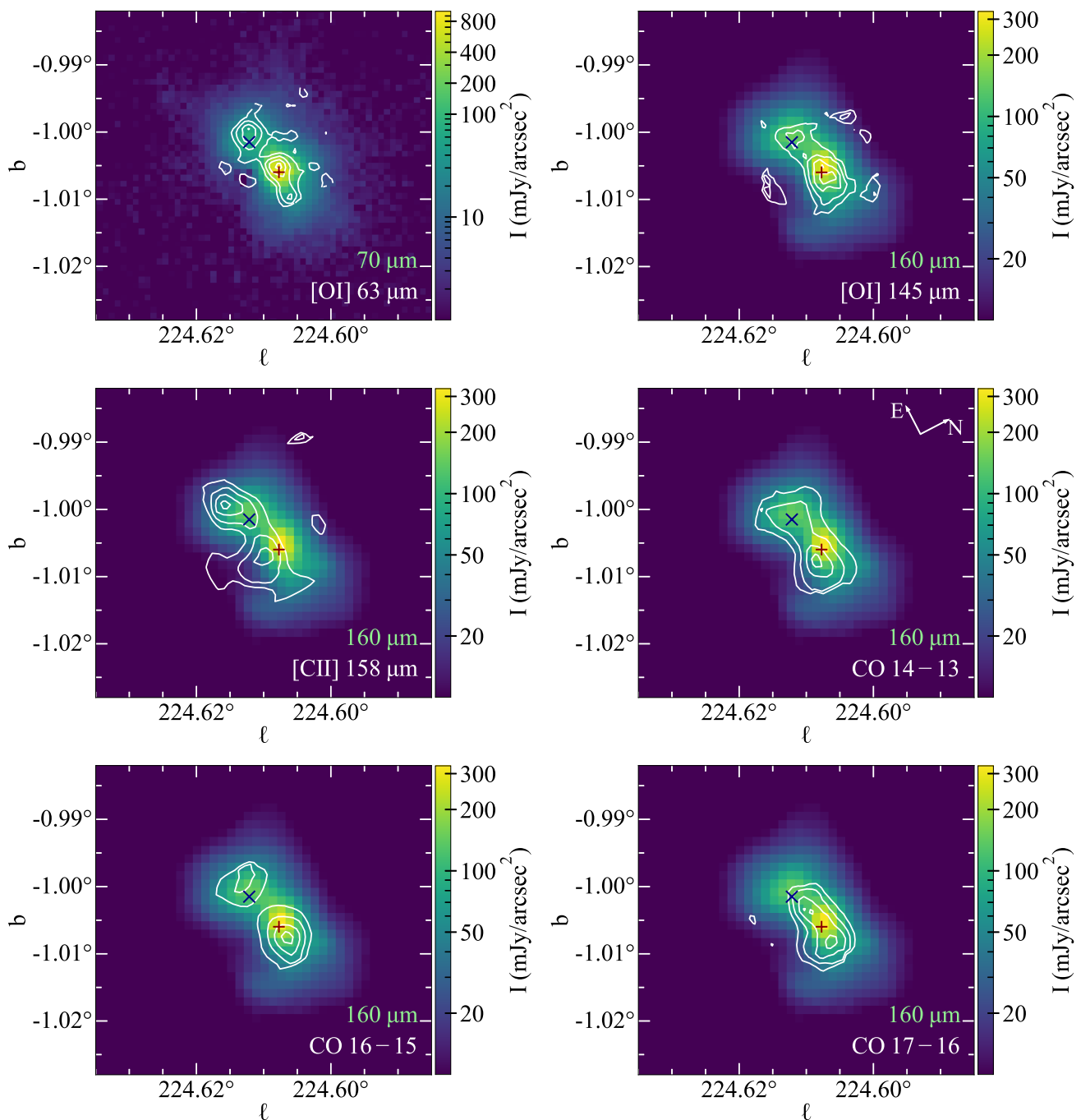


Fig. 4: FIFI-LS contour maps of the [O I] lines at 63.2 and 145.5  $\mu\text{m}$ , the [C II] line at 157.7  $\mu\text{m}$ , the CO lines with  $J_{\text{up}} = 14, 16, 17$  at 186, 163, and 153  $\mu\text{m}$  respectively (white contours) on top of the continuum emission at 160  $\mu\text{m}$  (at 70  $\mu\text{m}$  for the [O I] line at 63.2  $\mu\text{m}$ ) from *Herschel*/PACS. The white contours show line emission at 25%, 50%, 75%, and 95% of the corresponding line emission peak. The “+” and “x” signs show the positions of the dense cores A and B.

### 3.2. Spatial extent of FIR line emission

The FIR range contains several important diagnostic lines, which provide information about the physical conditions and processes that strongly contribute to the gas cooling (Goldsmith & Langer 1978; Kaufman & Neufeld 1996b). The analysis of spatial extent of various FIR species pinpoints the presence of shocks and/or UV radiation associated with star formation.

Figures 4 and 5 show the spatial extent of the FIR lines detected toward Gy 3–7 (Section 3.1). The line emission is compared to the FIR dust continuum emission at 70 or 160  $\mu\text{m}$

from *Herschel*/PACS (Figure 4) and the 4.5  $\mu\text{m}$  continuum tracing warmer dust from *Spitzer*/IRAC (Figure 5). Bright rotationally excited H<sub>2</sub> emission associated with shocks might also contribute to the flux in the 4.5  $\mu\text{m}$  IRAC band (Cyganowski et al. 2008, 2011). Appendix B shows additional maps of Gy 3–7 for lines from various species.

The high- $J$  CO emission distribution is elongated in the same direction as the IR continuum, but its peaks are offset from the continuum peaks at wavelengths similar to those of the respective CO lines. A similar pattern of emission is also seen for

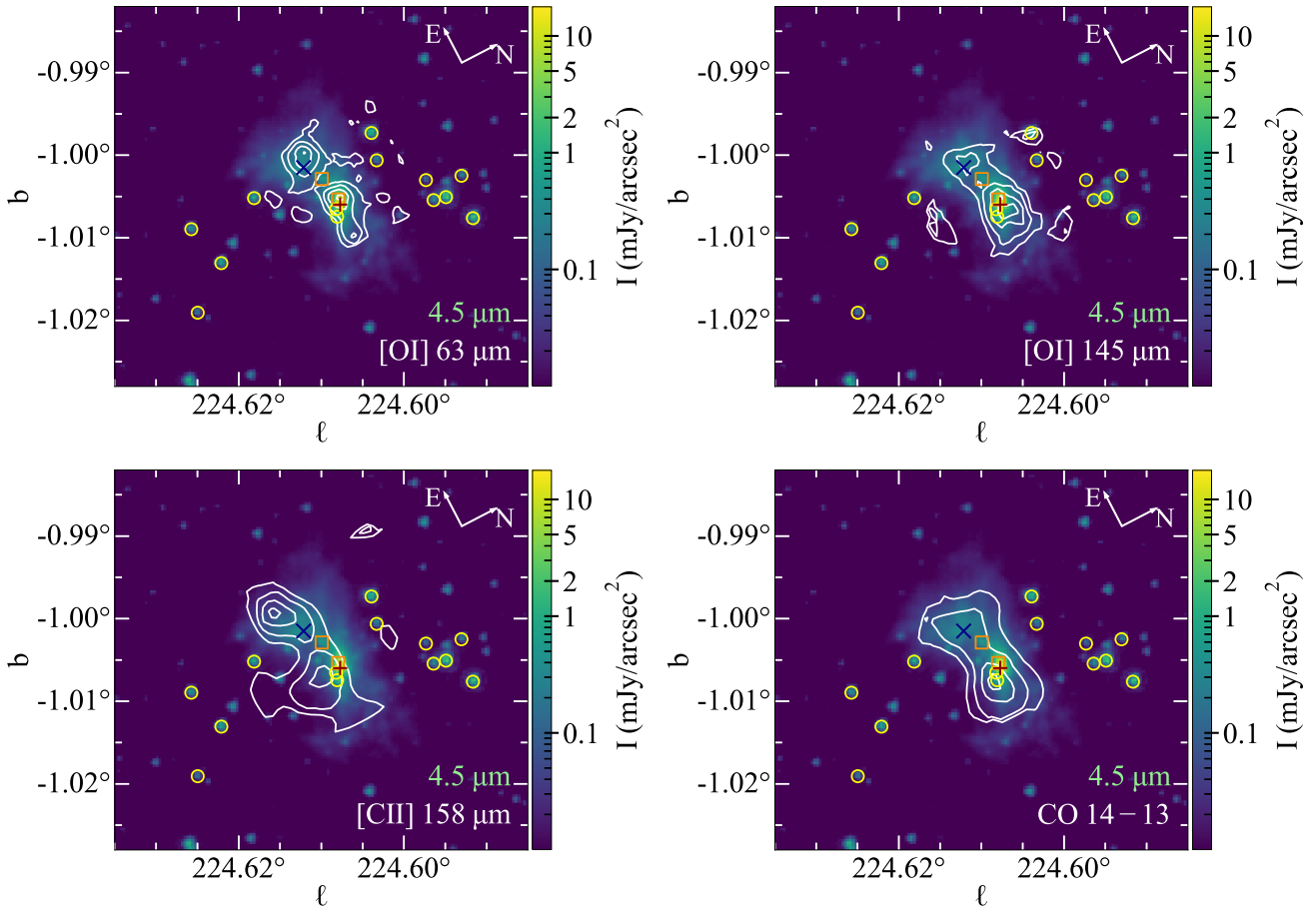


Fig. 5: FIFI-LS contour maps of the [O I] lines at 63.2 and 145.5  $\mu\text{m}$ , the [C II] line at 157.7  $\mu\text{m}$ , and the CO 14 – 13 line at 186  $\mu\text{m}$  (white contours) on top of the continuum emission at 4.5  $\mu\text{m}$  from *Spitzer*/IRAC. The contours show line emission at 25%, 50%, 75%, and 95% of the corresponding line emission peak. The “+” and “x” signs show the positions of the dense cores A and B, respectively. The orange squares show the positions of two YSO candidates with envelopes, and the yellow circles show the positions of the remaining YSOs (Section 4.5).

the [O I] 63  $\mu\text{m}$  and 145  $\mu\text{m}$  lines; yet, the peak of the [O I] lines are almost co-spatial with the core positions, which is not the case for the CO lines. Nevertheless, both the CO and the [O I] extend beyond the core positions along the E–W direction. Such elongated high- $J$  CO morphologies have been commonly interpreted as arising in shocked outflows from LM and IM protostars (Goicoechea et al. 2012; He et al. 2012; Kristensen et al. 2012; Karska et al. 2013; Matuszak et al. 2015; Green et al. 2016; Tobin et al. 2016; Kristensen et al. 2017b). Similarly, extended [O I] emission has been associated with embedded, atomic outflows (Karska et al. 2013; Nisini et al. 2015), as recently confirmed by detections of broad line wings in the 63  $\mu\text{m}$  line with SOFIA/GREAT (Leurini et al. 2015; Kristensen et al. 2017a; Yang et al. 2022a). Thus, the high- $J$  CO and [O I] emission toward Gy 3–7 might also arise from outflows, where shocks and UV radiation both contribute to gas cooling (see Section 5).

The [C II] emission also follows the pattern of the continuum emission, but its two emission peaks are offset by  $\sim 11''$  in different directions from the corresponding [O I] 63  $\mu\text{m}$  peaks. These differences are illustrated further in Figure 6, in which emission in various species is directly compared. Clearly, the [C II] emission traces different regions of Gy 3–7 than the high- $J$  CO and [O I] lines, which is at least partly due to its lower critical density,  $n_{\text{crit}} \sim (3.7\text{--}4.5)\times 10^3 \text{ cm}^{-3}$  for  $T_{\text{kin}}$  of 300–100 K (assum-

ing collisions with  $\text{H}_2$ , Wiesenfeld & Goldsmith 2014). As a result, [C II] is excited in lower density regions and likely exposed to external UV radiation creating a photodissociation region (Hollenbach & Tielens 1997). To some extent, the pattern of [C II] emission might be also affected by self-absorption, which is spectrally-unresolved in the FIFI-LS data (Section 3.1).

## 4. Analysis

The high- $J$  CO emission allows us to measure the CO rotational temperature of the warm molecular gas and to estimate the total line cooling by the FIR CO lines. The mapping capabilities of FIFI-LS provide information about the spatial distribution of the temperature and gas cooling across the entire clump.

### 4.1. CO rotational temperatures

We used Boltzmann (or rotational) diagrams to calculate the CO rotational temperature toward the two dense cores in Gy 3–7 as a proxy of gas kinetic temperature. Assuming that all these lines are optically thin and thermalized, their upper level column densities,  $N_u$ , are estimated using Eq. 1 following Goldsmith &

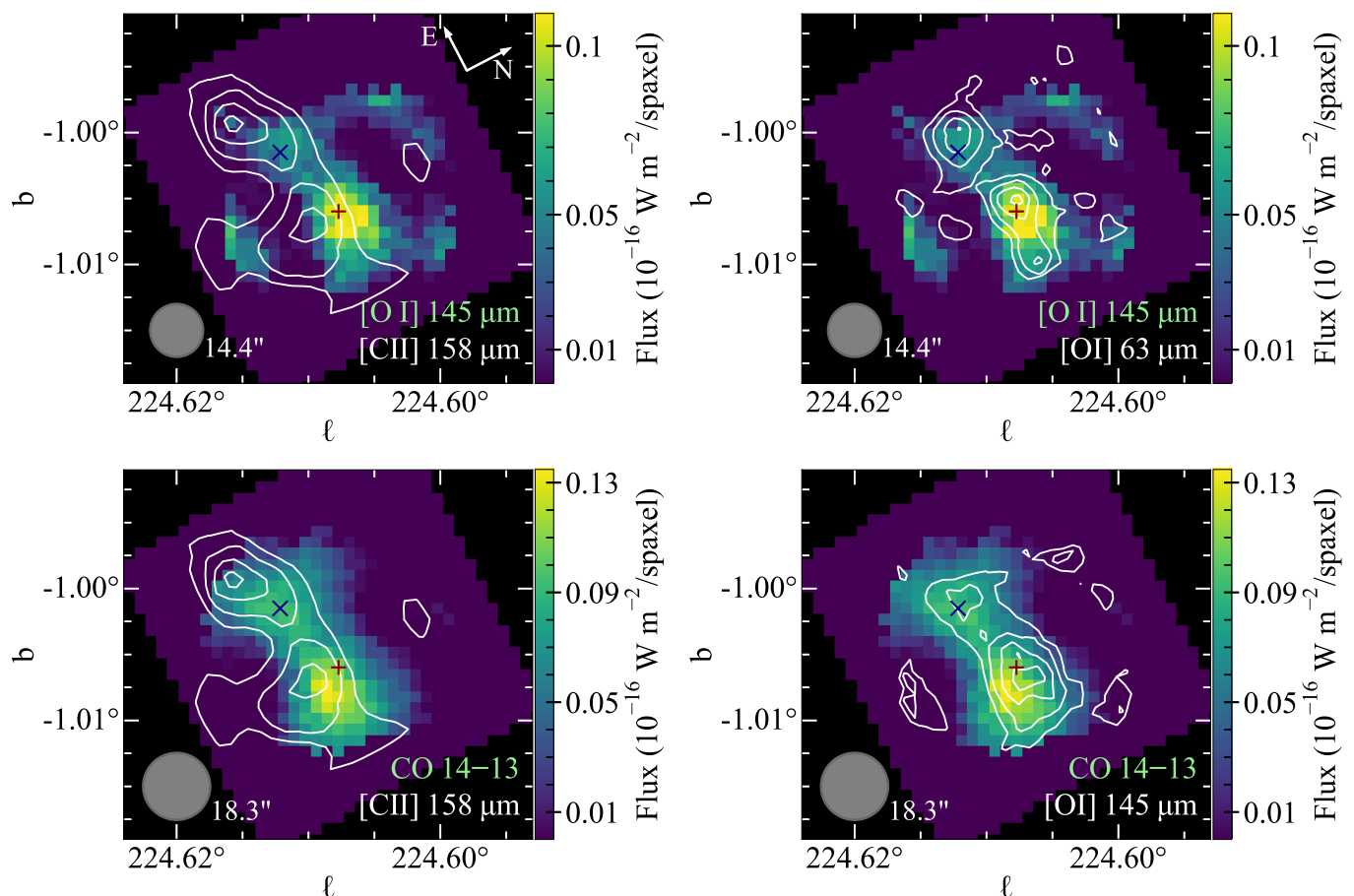


Fig. 6: Integrated intensity maps of selected pairs of FIR lines from FIFI-LS with the top line shown in colors, and the bottom line in white contours. The contour levels are 25%, 50%, 75%, and 95% of the corresponding line emission peak. The “+” and “x” signs show the positions of the dense cores A and B, respectively. The spaxel size in the emission map of the [O I] line at 63  $\mu\text{m}$  is 6''  $\times$  6'' (blue channel) and in the map of other lines (CO 14 – 13, [O I] at 145  $\mu\text{m}$ , and [C II] at 157.7  $\mu\text{m}$ ) is 12''  $\times$  12'' (red channel). Gray circles show the beam size for each color map.

Langer (1999):

$$\ln \frac{N_u}{g_u} = \ln \frac{N_{\text{tot}}}{Q(T_{\text{rot}})} - \frac{E_u}{k_B T_{\text{rot}}}, \quad (1)$$

where  $g_u$  is the degeneracy of the upper level,  $Q(T_{\text{rot}})$  is the rotational partition function at a temperature,  $T_{\text{rot}}$ ,  $N_{\text{tot}}$  is the total column density, and  $k_B$  is the Boltzmann constant (see Table 1).

Due to the low spatial resolution of FIFI-LS, the emitting region of the highly-excited gas is unresolved and thus we calculate instead the number of emitting molecules,  $N_u$ , for each transition (see e.g., Herczeg et al. 2012; Karska et al. 2013):

$$N_u = \frac{4\pi d^2 \lambda F_\lambda}{A h c}, \quad (2)$$

where  $F_\lambda$  is the flux of the line at wavelength  $\lambda$ ,  $d$  is the distance to Gy 3–7,  $A$  is the Einstein coefficient,  $c$  is the speed of light, and  $h$  is the Planck’s constant. Consequently, the total number of emitting molecules  $N_{\text{tot}}$  is derived instead of the  $N_{\text{tot}}$  from Eq. 1. To measure  $T_{\text{rot}}$  over the same physical scales, we convolved the CO emission maps down to the lowest spatial resolution corresponding to CO 14 – 13 observation (18.3'', see Table 1) and resampled the maps to the same pixel size. The flux of CO lines toward cores A and B was calculated within a beam of 20''

(see Table B.1). We performed a linear fit on the rotational diagram using the `curve_fit` function in Python ( $y = ax + b$ ). The  $T_{\text{rot}}$  and  $N_{\text{tot}}$  values are derived from the slope  $a$  and y-intercept  $b$  of the fit (Eq. 1).

Figure 7 shows the CO Boltzmann diagrams toward the two cores in Gy 3–7. We obtain rotational temperatures of  $305 \pm 85$  K and  $155 \pm 20$  K toward dense cores A and B, respectively, using CO lines with  $J_{\text{up}}$  of 14 – 22 (see Table 2). The same transitions have been associated with the “warm” component detected on CO diagrams toward protostars in the inner Galaxy and corresponding to the widely found  $T_{\text{rot}}$  of 300 K (Karska et al. 2013; Manoj et al. 2013; Green et al. 2013). The CO 30 – 29 and CO 31 – 30 data at 87.2 and 84.4  $\mu\text{m}$ , respectively, indicate the presence of the “hot” component toward core A (Karska et al. 2013). However, the 84.4  $\mu\text{m}$  line is blended with OH, which clearly affects the CO line flux (see Figure 3). Consequently, we are not able to constrain the “hot” component using only the CO 30-29 line.

The spatial distribution of the “warm” component’s CO rotational temperature toward the entire Gy 3–7 clump is shown in the left panel of Figure 8. Here, we calculate  $T_{\text{rot}}$  using the three lowest transitions ( $J_{\text{up}}$  of 14 – 17), which are detected in a large part of the map, except for the map edges where even CO 17 – 16 is not detected (Figure 4). The resulting  $T_{\text{rot}}$  values range from 105 to 230 K across the map, with a median value of



Table 2: CO rotational temperature, the number of emitting molecules, and total line luminosities of CO and [O I] lines toward dense cores in Gy 3–7 and IM YSOs from Matuszak et al. (2015)

Source	$T_{\text{rot}}^a$ (K)	$\log N_{\text{tot}}^a$	$L_{\text{CO(warm)}}^b$	$L_{[\text{O I}]63\mu\text{m}}$ ( $10^{-3}L_{\odot}$ )	$L_{[\text{O I}]145\mu\text{m}}$
Dense cores in Gy 3–7					
Core A	$305 \pm 85$	$50.41 \pm 0.34$	$73.31 \pm 19.69$	$92.69 \pm 5.01$	$8.38 \pm 0.29$
Core B	$155 \pm 20$	$50.96 \pm 0.24$	$30.47 \pm 6.10$	$76.17 \pm 5.37$	$6.15 \pm 0.37$
IM YSOs in the inner Milky Way					
AFGL 490 <sup>c</sup>	$255 \pm 25$	$51.11 \pm 0.13$	$225.17 \pm 19.85$	$336.65 \pm 1.47$	$29.56 \pm 0.24$
L1641	$270 \pm 35$	$50.06 \pm 0.17$	$24.31 \pm 2.74$	$14.69 \pm 0.14$	$1.20 \pm 0.05$
NGC 2071	$295 \pm 20$	$51.23 \pm 0.10$	$425.38 \pm 26.11$	$312.72 \pm 0.91$	$21.59 \pm 0.13$
Vela 17	$215 \pm 25$	$51.08 \pm 0.17$	$125.56 \pm 15.44$	$369.84 \pm 1.33$	$77.85 \pm 0.21$
Vela 19	$255 \pm 20$	$50.66 \pm 0.10$	$86.00 \pm 9.27$	$130.69 \pm 0.70$	$13.60 \pm 0.09$
NGC 7129	$295 \pm 35$	$50.84 \pm 0.14$	$187.26 \pm 19.16$	$66.03 \pm 0.78$	$3.13 \pm 0.88$

**Notes.** <sup>(a)</sup>  $T_{\text{rot}}$  and  $N_{\text{tot}}$  calculated using only CO 14 – 13, CO 16 – 15, CO 18 – 17, and CO 22 – 21 transitions for more direct comparisons with the cores in Gy 3–7. <sup>(b)</sup> The CO line luminosity in the "warm" component is obtained using all transitions reported in Matuszak et al. (2015) with  $J_{\text{up}}$  from 14 to 24 (see Section 4.2). <sup>(c)</sup> We adopted the new distance of 0.97 kpc toward this source when calculating  $T_{\text{rot}}$ ,  $N_{\text{tot}}$ , and luminosity of CO and [O I] lines (see Table D.2 and references therein).

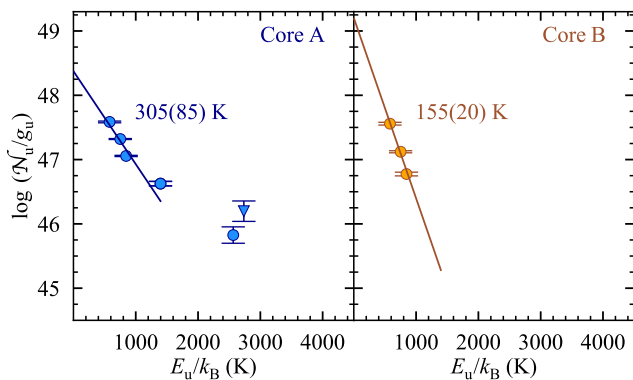


Fig. 7: CO rotational diagrams toward core A (left, in blue) and B (right, in orange). Circles refer to values based on line detections and the triangle shows the measurement using the upper limit of the CO 31–30 line, which is blended with OH. Solid lines show fits using transitions belonging to the "warm" gas component; the CO 30 – 29 line at  $87.19 \mu\text{m}$  is therefore not included. The CO rotational temperature  $T_{\text{rot}}$  derived from the rotational diagram is labeled in each panel and the value in parenthesis indicates its uncertainty.

$170(15) \pm 30 \text{ K}^5$ . The CO rotational temperatures are the highest in the vicinity of the CO 17 – 16 emission peaks, which are offset by  $\sim 17''$  from core A to the west (Figure 4). The morphology of the  $T_{\text{rot}}$  distribution suggests the origin of high- $J$  CO in a bipolar outflow driven by core A. Significantly lower CO temperatures,  $\leq 150 \text{ K}$ , are measured in the surroundings of core B, without a clear outflow signature from this object. The temperatures around 200 K at the eastern edge of the map are likely caused by higher gas densities in this region, rather than higher gas kinetic temperatures.

The spatial distribution of dust temperatures  $T_{\text{dust}}$  toward Gy 3–7, adopted from the *Herschel*/Hi-GAL survey, is also shown in the right panel of Figure 8. The morphology of regions

<sup>5</sup> The temperature in the bracket shows the mean error of the  $T_{\text{rot}}$  distribution and  $\pm 30$  refers to the standard deviation of the  $T_{\text{rot}}$  values.

with elevated temperatures is similar to the extent of  $N(\text{H}_2)$ , and shows two peaks at 27 and 21 K toward core A and B, respectively. The pattern differs significantly from the distribution of warm,  $\sim 300 \text{ K}$  gas, traced by CO lines, favoring the origin of the CO emission in a bipolar outflow driven by core A. Nevertheless, the lowest- $J$  CO transitions observed with FIFI-LS might partly trace the extended continuum emission, for instance, on the eastern part of Gy 3–7. We discuss this issue further in Section 5.1.

## 4.2. FIR line cooling

The FIR line cooling budget in LM protostars is sensitive to a source's evolutionary stage and  $L_{\text{bol}}$ , and its contributions provide important information on the shock origin of the FIR emission (Karska et al. 2013, 2018). Here, we quantify the luminosity of the FIR CO and [O I] lines toward the two cores in Gy 3–7 and a sample of IM protostars observed with *Herschel*/PACS (Matuszak et al. 2015).

### 4.2.1. Calculation procedure

We calculated the line cooling following procedures developed for *Herschel*/PACS observations in the same wavelength range (Karska et al. 2018). Briefly, we determined the line luminosity of CO lines in the "warm" component,  $L_{\text{CO(warm)}}$ , from the sum of the individual line fluxes with  $J_{\text{up}}$  from 14 to 24, corresponding to  $E_u/k_B = 580\text{--}1800 \text{ K}$ . Since not all CO transitions are observed, we use linear fits from the Boltzmann diagram to the "warm" component to recover the fluxes of the transitions not covered by FIFI-LS or PACS observations. The flux uncertainties of those transitions were propagated from the parameters of the linear fit and their uncertainty. The same procedure could be applied to the "hot" component toward Gy 3–7 cores due to the lack of data on a sufficient number of high- $J$  CO transitions. As a result, we did not calculate the total FIR CO cooling, that is, we did not account for transitions with  $E_u > 1800 \text{ K}$ . The advantage of this approach is that we avoid significant source-to-source variations in  $L_{\text{CO(hot)}}$ , which is reflected by the broad range of rotational temperatures measured using the highest- $J$

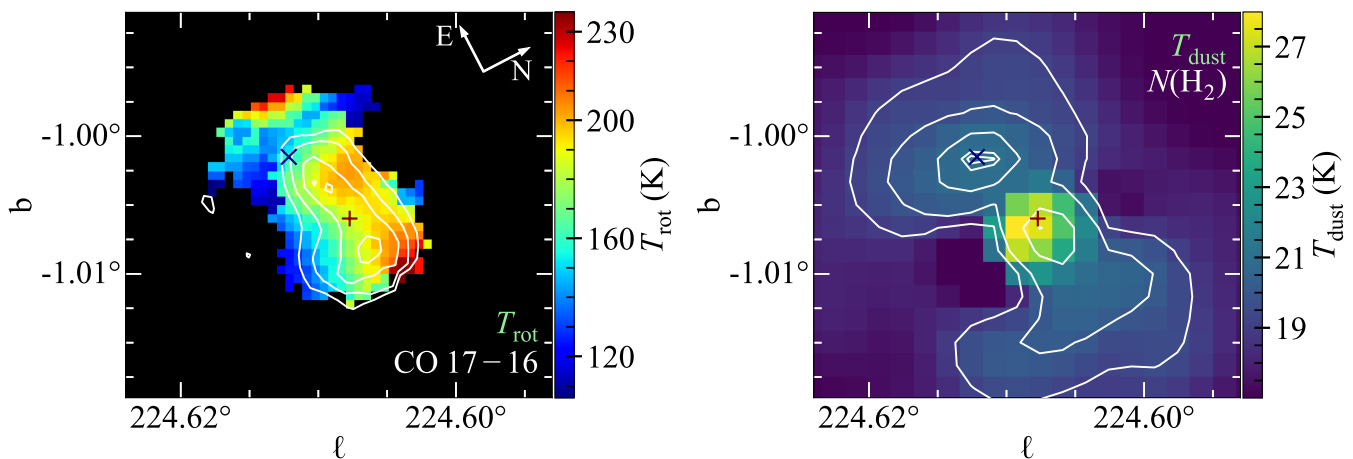


Fig. 8: Gas and dust temperatures toward Gy 3–7. Left: CO rotational temperature map obtained using Boltzmann diagrams. White contour map shows the CO 17 – 16 emission at 25%, 50%, 75%, and 95% of the emission peak. Right:  $\text{H}_2$  column density contour map overlaid on the dust temperature map derived from the pppmap tool with the *Herschel*/Hi-GAL survey (Marsh et al. 2017). Contour levels of the  $N(\text{H}_2)$  are at  $(5, 10, 30, 50, 55) \times 10^{21} \text{ cm}^{-2}$ .

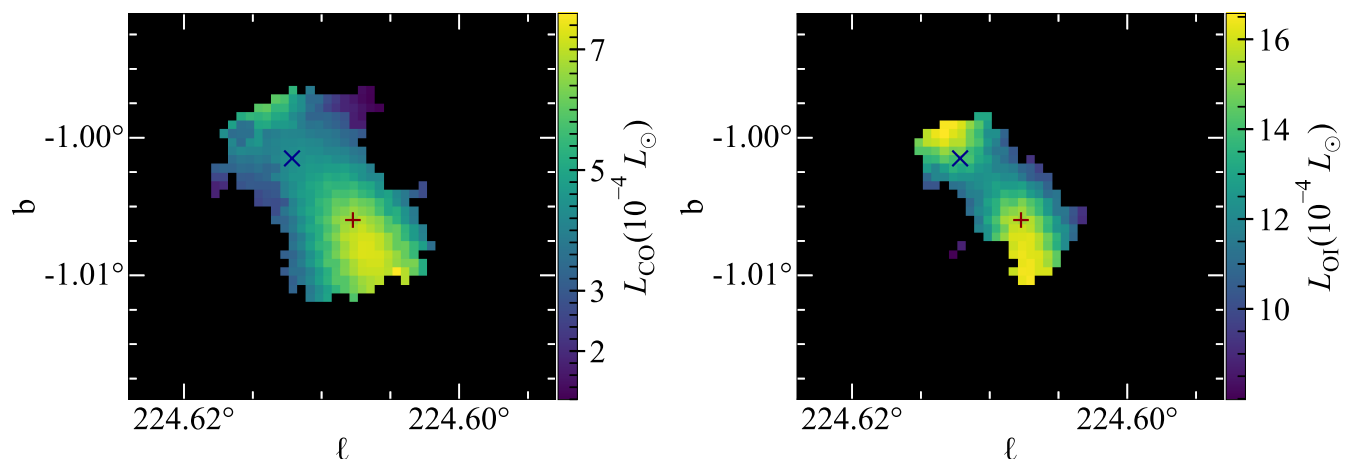


Fig. 9: Spatial extent of FIR line luminosities of CO (left) and [O I] (right) toward Gy 3–7. The calculation procedure is described in Section 4.2.

CO lines (see Figure 6 in Karska et al. 2018). The total line luminosity of [O I],  $L_{[\text{O I}]}$ , is calculated by the addition of the fluxes of the [O I] 63 and 145  $\mu\text{m}$  lines. Table 2 shows the FIR line luminosities obtained for Gy 3–7, as well as those for six IM YSOs from Matuszak et al. (2015).

Figure 9 shows the spatial distribution of the FIR line luminosity of CO and [O I] toward Gy 3–7. Most of the CO luminosity originates in a region west of core A, suggesting an outflow origin (see also Section 3.2). A similar region is characterized also by a high [O I] luminosity, which typically follows the pattern of high- $J$  CO emission around LM protostars (Karska et al. 2013; Nisini et al. 2015; van Dishoeck et al. 2021). Additionally, a high [O I] luminosity is measured to the east from core B, toward the direction of the [C II] peak (see Figures. 5 and 6). The lack of enhancement of CO line luminosity in this region could suggest an origin of the [O I] emission in the PDR. We explore this scenario further in Section 4.3.

#### 4.2.2. Flux correlations

We compare the FIR line emission in Gy 3–7 with the data based on *Herschel*/PACS measurements toward LM Class 0 and Class I (Karska et al. 2018), IM (Matuszak et al. 2015), and HM YSOs (Karska et al. 2014a). CO luminosities are consistently calculated for the "warm" component on Boltzmann diagrams. The correlations between luminosities of the two [O I] lines, as well as the [O I] and CO lines are shown in Figure 10.

A strong power-law correlation is found between the [O I] line luminosities for all low- and intermediate-mass sources including the two cores in Gy 3–7 (the Pearson coefficient of the correlation is  $r = 0.996$ , which corresponds to a significance of  $8.2\sigma$ ). The observed ratios of the [O I] 63  $\mu\text{m}$ /145  $\mu\text{m}$  lines span a range from 4 to 38 with a median value of  $\sim 12$ . These results are quantitatively similar to those shown in Figure 11 of Karska et al. (2013) for a sub-sample of 18 LM YSOs.

The HM YSOs follow a similar trend, however, several sources show a flux deficit in the [O I] 63  $\mu\text{m}$  line, which is likely caused by line-of-sight contamination and optical depth effects (see, e.g., Liseau et al. 1992; Leurini et al. 2015). A power-law

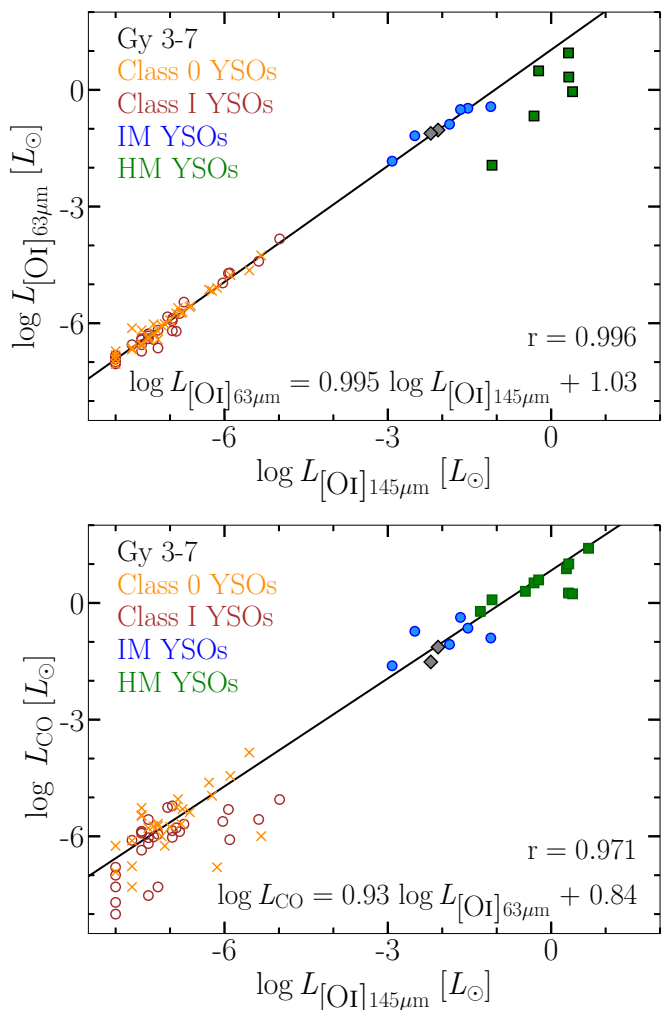


Fig. 10: Correlations between luminosities of FIR CO and [O I] lines. Top: Correlation between the luminosities of the 63 and 145  $\mu\text{m}$  [O I] lines at from LM to HM YSOs. Cores A and B in Gy 3–7 are marked as grey diamonds, Class 0 and Class I YSOs as orange "x" signs and red circles (Karska et al. 2018), respectively, IM YSOs as blue circles (Matuszak et al. 2015), and HM YSOs as green squares, respectively (Karska et al. 2014a). Black solid line is the linear fit to all sources except for the HM YSOs, showing a strong correlation between the two [O I] line luminosities. Bottom: Correlation between luminosities of the CO lines and the [O I] line at 145  $\mu\text{m}$ . Black solid line shows the linear fit to all sources, including the HM YSOs.

fit to the sample including HM YSOs shows a shallower slope ( $b = 0.91$  versus  $b = 0.99$ , when only LM and IM YSOs are considered). The correlation strength is comparable to the one for LM and IM sources alone, with a Pearson coefficient of 0.991 corresponding to  $8.5\sigma$ .

The CO line luminosity in the "warm" component shows a strong correlation with the 145  $\mu\text{m}$  [O I] line luminosity. A power-law fit to the entire sample returns a slope of  $b \sim 0.93$  and the Pearson coefficient of 0.971, corresponding to  $\sim 8.2\sigma$  (Figure 10). Clearly, the line luminosity of the [O I] 145  $\mu\text{m}$  line shows a smaller scatter for the HM YSOs with respect to the 63  $\mu\text{m}$  line. In case of LM YSOs, a significant scatter in the ratio of CO and [O I] line luminosities is likely linked to their different

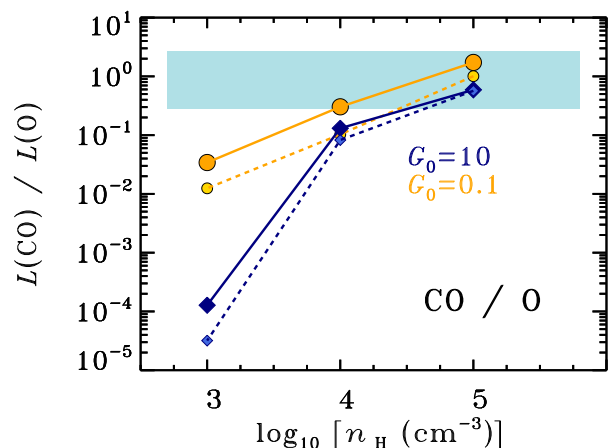


Fig. 11: Ratio of the CO and [O I] luminosities as a function of pre-shock density for UV irradiated C-shock models and observations of Gy 3–7 cores and IM YSOs from Matuszak et al. (2015) (light blue box). All models correspond to UV fields parameterized by  $G_0$  of 10 (in blue) and 0.1 (in orange). Solid lines connect models with shock velocities  $v_s$  of 20  $\text{km s}^{-1}$ , and dashed lines – the models with  $v_s$  of 10  $\text{km s}^{-1}$ .

evolutionary stages. The ratio of CO line luminosity over  $L_{\text{bol}}$  is  $\sim 2.3$  larger for Class 0 than Class I sources, whereas the [O I] luminosities are similar for both groups (Karska et al. 2018). Thus, the molecular-to-atomic line cooling is expected to be higher in Class 0 objects. Indeed, the linear fit using only Class 0 sources results in a shallower slope, but do not affect the general conclusions.

In summary, we find a strong correlation between the line luminosities of the [O I] and CO lines for YSOs in a broad mass range, consistent with previous results for LM YSOs (Karska et al. 2013). Combined with the similar spatial extent of the [O I] and CO lines (Section 3.2), the correlations suggest a similar physical origin of the two species.

#### 4.3. Properties of a possible photodissociation region

Assuming that the [O I] and [C II] lines predominately arise from a photodissociation region (PDR), the UV field strengths,  $G_0$ , and hydrogen nucleus number densities,  $n_{\text{H}}$ , across Gy 3–7 can be obtained from their ratios. These assumptions might be justified in case of the eastern part of Gy 3–7 with relatively weak CO line luminosities (see Section 4.2). On the contrary, the [O I] line luminosity in the surrounding of core A closely follows the high- $J$  CO emission associated with outflow shocks.

We determined the physical properties of the PDR using the PDR Toolbox 2.1.1<sup>6</sup> (Pound & Wolfire 2011) based on the PDR models provided by Kaufman et al. (2006). We used three line ratios involving the [O I] lines at 63.2  $\mu\text{m}$  and 145.5  $\mu\text{m}$ , and [C II] line at 157.7  $\mu\text{m}$ , and ran the code at each spaxel of the FIFI-LS maps. We obtained gas densities of  $10^4$ – $10^5 \text{ cm}^{-3}$  and UV field strengths of the order of  $10^3$ – $10^6$  times the average interstellar UV radiation field (Habing 1968). These physical conditions are typical for dense, star-forming clumps associated with HM YSOs (Ossenkopf et al. 2010; Benz et al. 2016; Mirocha et al. 2021). However, given that Gy 3–7 is associated with IM

<sup>6</sup> <https://dustem.astro.umd.edu/>

YSOs (see Section 4.5), UV radiation fields of  $10^3$  or higher are unlikely (e.g., Karska et al. 2018).

The similar spatial extent of the [O I] and high- $J$  CO emission (Section 3.2) and the strong line luminosity correlation between the two species (Section 4.2) favor the origin of the bulk of [O I] in the outflow shocks rather than in the photodissociation region. We consider this scenario in Section 4.4.

#### 4.4. Comparisons with UV-irradiated shocks

Bright FIR emission detected toward LM YSOs has been interpreted in the context of continuous ( $C$ -type) shocks irradiated by UV photons (Karska et al. 2014b, 2018; Kristensen et al. 2017b). Figure 11 shows a comparison of the FIR observations toward IM YSOs, including two cores in Gy 3–7, and the UV-irradiated shock models from Melnick & Kaufman (2015) and Karska et al. (2018).

Predictions of shock models were previously calculated for high- $J$  CO lines covered by *Herschel*/PACS. Here, we show the predictions for UV field strengths,  $G_0$ , of 0.1 and 10, and shock velocities of 10 and 20 km s $^{-1}$  (see also Fig. 14 in Karska et al. 2018). For the sake of comparison, we calculated the total FIR line luminosity of CO using the transitions in the "warm" component (Section 4.2.1), as well as high- $J$  CO lines, both for Gy 3–7 and for IM YSOs (Matuszak et al. 2015). The [O I] line luminosity is calculated from the sum of the two fine-structure [O I] lines.

The models show a good match with observations for pre-shock H $_2$  number densities of  $10^5$  cm $^{-3}$  and the entire range of the considered UV radiation field strengths. For shock velocities,  $v_s$ , of 20 km s $^{-1}$ , a possible match is also found for pre-shock densities of  $10^4$  cm $^{-3}$  and  $G_0$  of 0.1. The compression factor  $>10$  is expected in  $C$ -type shocks (Karska et al. 2013), so the gas densities are of the order of  $10^5$ – $10^6$  cm $^{-3}$ , in agreement with those of LM YSOs (e.g., Kristensen et al. 2012; Mottram et al. 2017).

Due to the lack of H $_2$ O observations from FIFI-LS and non-detections of OH, we are limited to comparisons between CO and [O I] lines. Some of the [O I] emission might arise in the PDR (Section 4.3), which would increase the observed line luminosity ratio; however, the strong correlation of [O I] and high- $J$  CO tracing outflow shocks does not support this scenario.

#### 4.5. Spectral energy distribution analysis

We investigate the physical properties of 15 individual YSO candidates from Tapia et al. (1997) and Sewilo et al. (2019) in Gy 3–7 to understand their possible impact on the FIR and submillimeter line emission. Spectral energy distribution (SED) models of YSOs from Robitaille (2017) are fitted to the multi-wavelength photometry of YSOs using a dedicated fitting tool (Robitaille et al. 2007). Multi-wavelength photometry spanning from near- to mid-IR range of YSO candidates in the IRAS field is presented in Appendix C.

We followed the procedures described in detail in Karska et al. (2022). We used 18 sets of model SEDs including various physical components of a YSO: star, disc, in-falling envelope, bipolar cavities, and an ambient medium (Robitaille 2017). We used the PARSEC evolutionary tracks produced by the revised Padova code (Bressan et al. 2012; Chen et al. 2014, 2015; Tang et al. 2014) to quantify the results of SED model fitting. Models producing YSO parameters outside of the PARSEC pre-main sequence (PMS) tracks were excluded. YSOs with models in line with the PARSEC tracks are illustrated on the Hertzsprung-

Russell diagram in Appendix C. For those YSOs, we calculate the stellar luminosity from the Stefan-Boltzmann law, using the stellar radius and effective temperature from the SED fitting. The masses and ages are determined from the closest PMS track; however, we only provide the stellar masses and ages that are consistent with the SED fitting results (i.e., the evolutionary stage) and YSO lifetimes from Dunham et al. (2015), respectively (see Section 3.7 in Karska et al. 2022).

Table 3 shows the best-fit SED models for 12 YSOs in Gy 3–7. The SEDs of two sources require an envelope contribution which is typical for deeply-embedded Class 0/I YSOs (see Figure 12), while six sources are successfully modeled with a passive disk and four are normal stars (see Appendix C). The resulting physical parameters determined from SED models are shown in Table 4.

The two YSOs with envelopes, No. 10 and 12 in Table 4, are located in the center of Gy 3–7 (see Figures 1 and 5), and their strong IR excess has already been noted by Tapia et al. (1997). The Class 0 YSO is co-spatial with the IRAS source and the dense core A (Elia et al. 2021), and might be the source of the outflow responsible for the FIR emission. Both objects are in the IM regime based on their luminosities obtained from SEDs. The four objects that are modeled as stars with foreground extinction have photometry only from 1 to 5  $\mu$ m. In this range, it is difficult to distinguish between stars with foreground extinction and stars with disks, so we do not rule out the latter explanation.

## 5. Discussion

Far-IR observations from FIFI-LS confirm the status of Gy 3–7 as a deeply-embedded cluster, as originally proposed by Tapia et al. (1997). Here, we discuss the likely origin of FIR emission in Gy 3–7 and we search for any effects coming from metallicity by comparison with YSOs from the inner Galaxy.

### 5.1. Origin of FIR emission in Gy 3–7

A strong correlation of high- $J$  CO and [O I] luminosities and their spatial extent in Gy 3–7 provides a strong support toward the common origin of the two species. The modeling of envelopes of HM YSOs showed that emission from shocks is necessary to reproduce line fluxes of high- $J$  CO lines (Karska et al. 2014a). The same is certainly the case for LM and IM YSOs as well, which are characterized by lower envelope densities and temperatures. On the other hand, the [O I] emission could be associated with a photodissociation region (Kaufman & Neufeld 1996a; Hollenbach & Tielens 1997) or outflow shocks (Karska et al. 2013; Nisini et al. 2015). Recent velocity-resolved profiles of the [O I] line at 63  $\mu$ m with SOFIA/GREAT support the later scenario for LM YSOs, which does not suffer from strong self-absorption (Kristensen et al. 2017a; Yang et al. 2022a). Therefore, we assume that the entire high- $J$  CO and [O I] emission originates from outflow shocks. As shown in Section 4.4, the line luminosity ratio of CO and [O I] is consistent with  $C$ -type shocks irradiated by UV fields of 0.1–10 times the average interstellar radiation field and pre-shock densities of  $10^4$ – $10^5$  cm $^{-3}$  (see also, Melnick & Kaufman 2015; Karska et al. 2018). The detection of variable H $_2$ O maser further confirms the outflow activity in the region (Furuya et al. 2003a). We provide details in Appendix A.

The physical conditions in Gy 3–7 are also constrained by CO rotational temperatures, which provide a good proxy of gas kinetic temperatures (Karska et al. 2013; van Dishoeck et al.



Table 3: Best-fit models of SED using the Robitaille (2017) classification

Model Set	# of sources	Components	Group
s--s-i	4	star	–
sp--s-i	2	star + passive disk; $R_{\text{inner}} = R_{\text{sub}}$	<i>d</i>
sp--h-i	4	star + passive disk; variable $R_{\text{inner}}$	<i>d</i>
s-pbhmi	1	star + power-law envelope + cavity + medium; variable $R_{\text{inner}}$	<i>e</i>
spubsmi	1	star + passive disk + Ulrich envelope + cavity + medium; $R_{\text{inner}} = R_{\text{sub}}$	<i>d + e</i>

**Notes:** Seven characters in the model set names indicate which component is present; they are (in order): s: star; p: passive disk, p or u: power-law or Ulrich envelope; b: bipolar cavities; h: inner hole; m: ambient medium; and i: interstellar dust. A dash (–) is used when a component is absent.  $R_{\text{inner}}$  is the inner radius for the disk, envelope, and the ambient medium - when one or more of these components are present.  $R_{\text{sub}}$  is the dust sublimation radius.

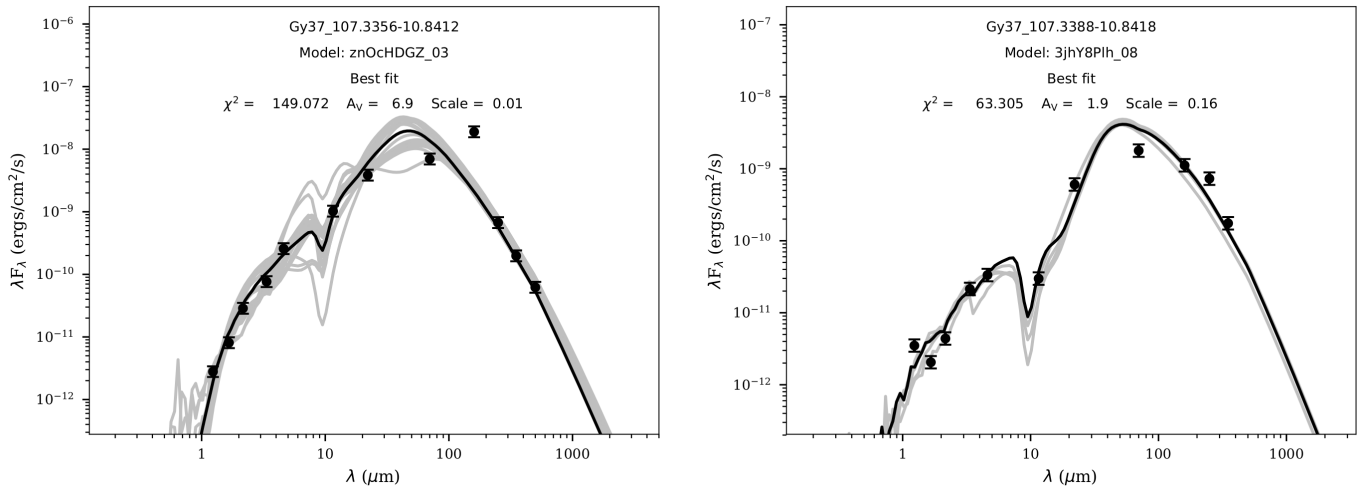


Fig. 12: SEDs of YSOs in Gy 3–7 well-fitted with Robitaille (2017) models with envelopes. The best fit model is indicated with the black solid line and gray lines show the YSO models with  $\chi^2$  between  $\chi^2_{\text{best}}$  and  $\chi^2_{\text{best}} + F \times n$ , where  $n$  is the number of data points and  $F$  is a threshold parameter which we set to 3 (Sewilo et al. 2019). Filled black circles are valid flux values with uncertainties. The values of a reduced  $\chi^2$  and interstellar visual extinction for the best-fit model are indicated in the plots. Appendix C shows the SEDs for the remaining YSOs in Gy 3–7.

Table 4: Physical parameters for a subset of YSO candidates with at least five photometric data points

ID	Model set <sup>a</sup>	Class	$R_*$ ( $R_{\odot}$ )	$T_*$ (K)	$L_*$ ( $L_{\odot}$ )	$M_*^b$ ( $M_{\odot}$ )	Age <sup>b</sup> (Myr)	Note <sup>c</sup>
1	sp-s-i	II/III	5.2	3592	4.0	...	...	
2	sp-s-i	II/III	2.6	6791	13.2	...	...	TP01
4	s-s-i	star	1.2	2955	0.1	...	...	
5	s-s-i	star	1.0	3388	0.1	...	...	
6	s-s-i	star	1.0	5120	0.6	...	...	TP03
9	sp-h-i	II/III	3.3	3359	1.2	...	...	
10	s-pbhmi	0	25.8	6214	892.1	8.0	0.06	TP06
11	s-s-i	star	1.2	2955	0.1	...	...	
12	spubsmi	I	23.0	6194	702.1	...	...	TP07
13	sp-h-i	II/III	2.6	6112	8.4	...	...	TP09
14	sp-h-i	II/III	3.6	3736	2.2	...	...	
15	sp-h-i	II/III	10.3	7101	244.9	...	...	TP08

<sup>a</sup> See Table 3 footnotes for the description of the model set names.

<sup>b</sup> We provide stellar masses ( $M_*$ ) and ages only for sources with reliable estimation of these parameters (see text for details).

<sup>c</sup> IDs of the YSO candidates in Gy 3–7 identified by Tapia et al. (1997), see Figure 1.

2021). The high- $J$  transitions are likely optically thin and thermalized at gas densities  $>10^5 \text{ cm}^{-3}$  that are routinely measured

for LM and IM YSOs (e.g., Kristensen et al. 2012; Mottram et al. 2017). The top panel in Figure 13 shows that  $T_{\text{rot,CO}}$  associated

with the two dense cores in Gy 3–7 is either fully consistent (core A) or at the low-end of other IM YSOs (core B), for which the median value from the literature is  $320(33) \pm 35$  K (Matuszak et al. 2015). Similar rotational temperatures have been measured for LM and HM YSOs (Karska et al. 2013, 2014a, 2018; Green et al. 2013, 2016; Manoj et al. 2013; Yang et al. 2018), with average values of  $328(33) \pm 63$  K (Karska et al. 2018) and  $300(23) \pm 60$  K (Karska et al. 2014a), respectively.

Some differences between the dense core B in Gy 3–7 and the other YSOs studied in the literature might result from a smaller number of transitions probed by FIFI-LS. The curvature seen in the rotational diagrams causes the rotational temperature to be underestimated if high- $J$  CO transitions are not observed. Therefore, we re-calculated all literature measurements of  $T_{\text{rot}}$  for IM and HM YSOs using the same or similar transitions as obtained for Gy 3–7 (Table 2 and Appendix D). As expected, CO rotational temperatures for IM and HM YSOs are now lower than reported in the literature and consistent even with core B (see bottom panel of Figure 13).

## 5.2. Possible impact of metallicity on FIR line emission in the outer Galaxy

Far-IR observations of HM YSOs in the low-metallicity environments of the SMC and LMC show a lower fraction of molecular-to-atomic emission with respect to Galactic YSOs (Oliveira et al. 2019). Here, we investigate the impact of bolometric luminosity,  $L_{\text{bol}}$ , and source Galactocentric radius,  $R_{\text{GC}}$ , on the ratio of CO and [O I] line luminosity.

Figure 14 shows the molecular-to-atomic ratio toward Gy 3–7 cores and other Galactic IM and HM YSOs as a function of  $L_{\text{bol}}$ . The values of  $L_{\text{bol}}$  for the two cores in Gy 3–7 are adopted from Elia et al. (2021), and are equal to 75.9 and 324.2  $L_{\odot}$ , respectively. The correlation is characterized by a Pearson coefficient of 0.19, corresponding to  $1.6\sigma$ . Since the number of LM YSOs exceeds by far the number of IM and HM sources, we also search for trends in the binned datasets. We bin sources in equal intervals of  $\log L_{\text{bol}}=1$ , and adopt a  $1\sigma$  variance of the distribution as the uncertainty inside the bin. As a result, we confirm a weak correlation between the ratio of line luminosity and  $L_{\text{bol}}$  ( $r \sim 0.59$ , corresponding to  $1.5\sigma$ ). Thus, our large sample of YSOs starts to reveal a relationship between the mass of YSOs and the fraction of molecular-to-atomic cooling. This has not been possible with a sample of 18 LM YSOs and 10 HM YSOs analyzed in Karska et al. (2014a), where a ratio of  $\sim 4$  was reported for YSOs in the entire mass regime. We note, however, that the *Herschel*/PACS measurements from the literature benefited from additional detections of H<sub>2</sub>O and OH, which were included in the molecular FIR cooling.

Figure 15 shows the molecular-to-atomic ratio as a function of Galactocentric radius. In addition, Figure 16 shows the same ratio as a function of metallicity,  $Z$ , estimated assuming elemental abundance gradients derived from H II regions (Balsler et al. 2011). Appendix D provides heliocentric distances, Galactocentric radii, and metallicities of Galactic sources, as well the measurements of CO and [O I] for YSOs in both the Milky Way and the Magellanic Clouds.

The molecular-to-atomic ratio decreases very weakly with the Galactocentric radius (Fig. 15) but the Pearson coefficient is too small to confirm the correlation ( $r = 0.08$ , corresponding to  $0.7\sigma$ ). Additional observations of YSOs in the outer Galaxy would be necessary to constrain the molecular-to-atomic ratio, in particular, in the gap between 10 and 12 kpc. Due to the lack of such observations, we searched for trends as a function of

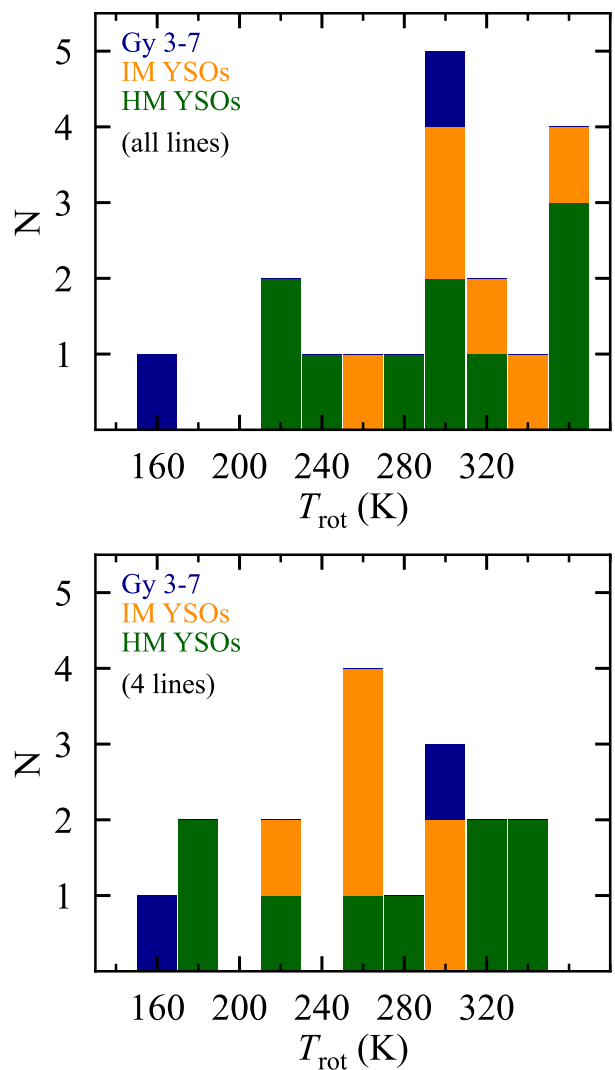


Fig. 13: CO rotational temperatures for dense cores in Gy 3–7 and intermediate- and high-mass YSOs from the literature (Karska et al. 2014a; Matuszak et al. 2015). Top: Straightforward comparison with the literature values. Bottom: Comparison accounting for the number of observed CO lines considered in the rotational diagrams.

metallicity by including YSOs in the Magellanic Clouds (Fig. 16). We note, however, that the [O I] line at 145  $\mu\text{m}$  was not observed toward sources in the Magellanic Clouds, and the ratio of the two [O I] lines calculated for LM YSOs from Karska et al. (2018) was adopted to estimate its fluxes (Oliveira et al. 2019). As seen in Figure 10, this ratio may differ for HM YSOs due to self-absorption or optical depth effects in the [O I] 63  $\mu\text{m}$  line. Additionally, the total CO luminosity of YSOs in the SMC and LMC was estimated using the detections in SPIRE and the conversion factor from Yang et al. (2018), also based on LM YSOs.

In conclusion, Gy 3–7 follows closely the correlations set by YSOs observed in the Milky Way and the Magellanic Clouds. The ratio of molecular-to-atomic line emission is dominated by source bolometric luminosities, and only a very weak decreasing trend with the Galactocentric radius was detected.

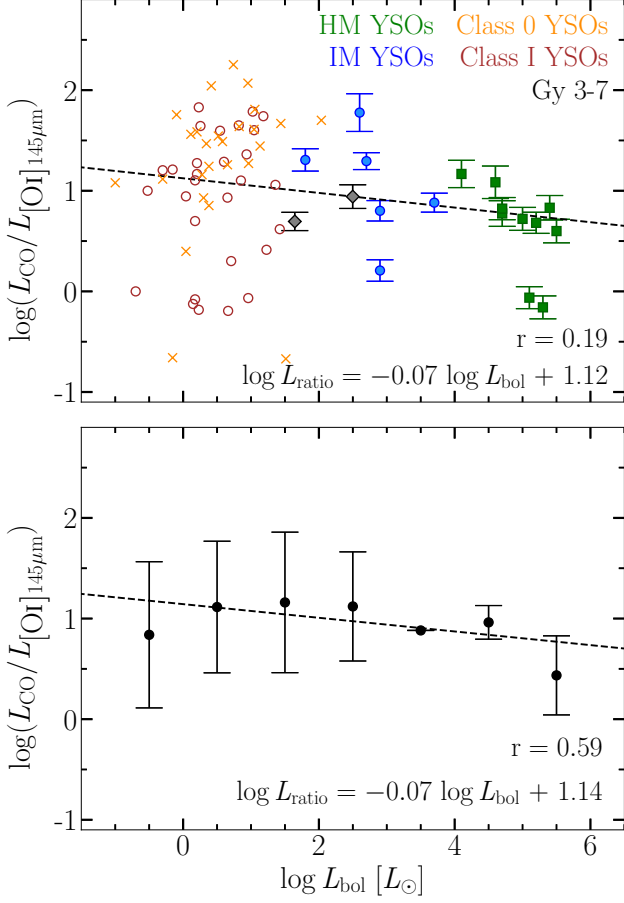


Fig. 14: Correlations between the ratio of CO and [O I] line luminosities and bolometric luminosity of YSOs in the two cores in Gy 3–7 (gray diamonds), Class 0 and Class I YSOs (orange ‘x’ signs and red circles, respectively; [Karska et al. 2018](#)), IM YSOs (blue circles; [Matuszak et al. 2015](#)), and HM YSOs (green squares; [Karska et al. 2014a](#)). The bolometric luminosities for Gy 3–7 cores are adopted from [Elia et al. \(2021\)](#). The top panel shows a power-law fit to all individual data points, and the bottom panel shows the fit to the data bins (both shown as black dashed line).

## 6. Conclusions

We investigated the SOFIA/FIFI-LS maps of the CO transitions from  $J = 14 - 13$  to  $J = 31 - 30$ , the [O I] lines at  $63.2 \mu\text{m}$  and  $145.5 \mu\text{m}$ , and the [C II]  $158 \mu\text{m}$  line toward the outer Galaxy cluster Gy 3–7. Spatial information on the FIR emission enabled us to quantify such physical parameters as temperatures, densities, and UV radiation fields, as well as to associate them with identified YSOs. Our conclusions are as follows:

- The CO  $J = 14 - 13$  to  $J = 16 - 15$  emission lines are detected in a significant part of Gy 3–7, where *Herschel*/PACS  $160 \mu\text{m}$  continuum emission is also strong. Higher- $J$  CO lines up to  $31 - 30$  are clearly detected only toward the dense core A.
- The spatial extent of the [O I] emission at  $63$  and  $145 \mu\text{m}$  is similar to that of CO  $14 - 13$  and the  $70$  and  $160 \mu\text{m}$  continuum emission. The [C II] emission is also extended, but shows systematic shifts in the emission peaks away from the FIR continuum, tracing lower density gas.
- The CO rotational diagrams show the warm components toward two cores with  $T_{\text{rot}}$  of  $305$  and  $155$  K, and a range of

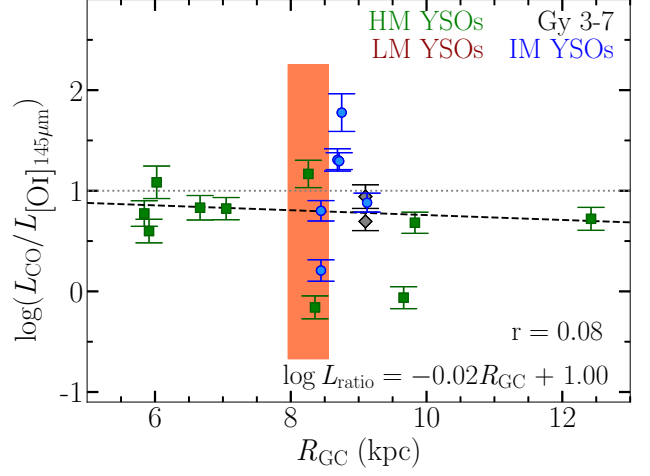


Fig. 15: Ratio of molecular to atomic line luminosities as a function of the Galactocentric radius. The light coral box indicates the range of the line luminosity ratio and the Galactocentric radius for LM YSOs in the nearby clouds, which are excluded from the power-law fit to the remaining YSOs (dashed black line). Gray dotted horizontal line indicates where the molecular luminosity is equal to the atomic luminosity.

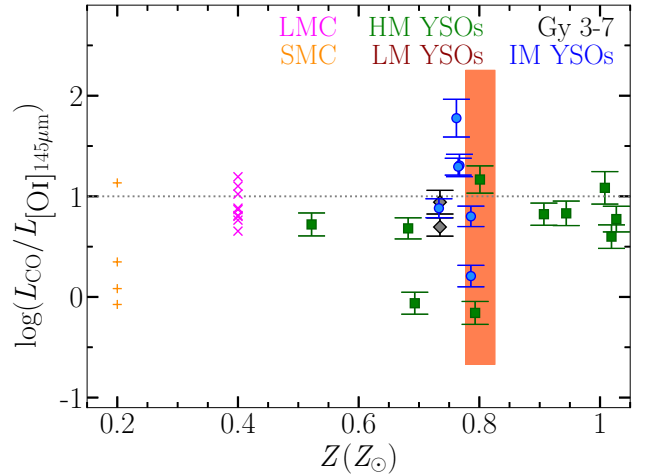


Fig. 16: Ratio of molecular to atomic line luminosities as a function of metallicity,  $Z$ . HM YSOs in the SMC and LMC are shown with cross and ‘x’ symbols in orange and purple colors, respectively. The light coral box indicates the range of the line luminosity ratio and the metallicity for LM YSOs in the nearby clouds, which are excluded from the power-law fit to the remaining YSOs (dashed black line). The gray dotted horizontal line indicates where the molecular luminosity is equal to the atomic luminosity.

$T_{\text{rot}}$  from  $\sim 105$  to  $230$  K throughout the cluster, where only three high- $J$  CO lines are unambiguously detected. Similar rotational temperatures have been detected toward IM and HM YSOs in the inner Milky Way calculated using the same or similar CO transitions.

- A strong correlation of the CO and [O I] line luminosities and their similar spatial extent point at the common origin in the outflow shocks. The CO / [O I] line luminosity ratio of Gy 3–7 cores and other intermediate-mass YSOs is consistent with C-type shocks propagating at pre-shock densities

- of  $10^4 - 10^5 \text{ cm}^{-3}$  and UV fields of 0.1-10 times the average interstellar radiation field.
- Physical parameters for 15 YSO candidates in the Gy 3–7 cluster are obtained from a YSO SED model fitting (Robitaille 2017). Two sources, corresponding to Hi-GAL dense cores from Elia et al. (2021), are well-fitted with YSO models including the envelope, confirming their early evolutionary stage (Class 0/I). The location of the Class 0 source at the center of Gy 3–7 cluster suggests that it might be the driving source of the outflow revealed by FIR emission.
  - The ratio of warm CO and [O I] at  $145 \mu\text{m}$  line luminosities from protostellar envelopes shows a weak decreasing trend with the bolometric luminosity and Galactocentric radius. We do not identify any significant dependence of the line cooling in Gy 3–7 on metallicity.

High-resolution submillimeter observations would be necessary to unambiguously associate FIR emission from FIFI-LS with candidate YSOs and their outflows. Alternatively, the efficient imaging of Gy 3-7 with the Mid-Infrared Instrument on board James Webb Space Telescope in F560W and/or F770 W filters tracing  $\text{H}_2$  emission would unveil the details in the outflows (Yang et al. 2022b).

*Acknowledgements.* NL, AK, MF, MG, MK, and KK acknowledge support from the First TEAM grant of the Foundation for Polish Science No. POIR.04.04.00-00-5D21/18-00 (PI: A. Karska). AK also acknowledges support from the Polish National Agency for Academic Exchange grant No. BPN/BEK/2021/1/00319/DEC/1. This article has been supported by the Polish National Science Center grant 2014/15/B/ST9/02111 and 2016/21/D/ST9/01098. The material is based upon work supported by NASA under award number 80GSFC21M0002 (MS). The research is supported by a research grant (19127) from VILLUM FONDEN (LEK). This work is based (in part) on observations made with the NASA/DLR Stratospheric Observatory for Infrared Astronomy (SOFIA). SOFIA is jointly operated by the Universities Space Research Association, Inc. (USRA), under NASA contract NNA17BF53C, and the Deutsches SOFIA Institut (DSI) under DLR contract 50 OK 2002 to the University of Stuttgart. The 32 m radio telescope is operated by the Institute of Astronomy, Nicolaus Copernicus University and supported by the Polish Ministry of Science and Higher Education SpUB grant.

## References

Arce, H. G., Shepherd, D., Gueth, F., et al. 2007, in *Protostars and Planets V*, ed. B. Reipurth, D. Jewitt, & K. Keil, 245

Balsler, D. S., Rood, R. T., Bania, T. M., & Anderson, L. D. 2011, *ApJ*, 738, 27

Benedettini, M., Molinari, S., Baldeschi, A., et al. 2020, *A&A*, 633, A147

Benz, A. O., Bruderer, S., van Dishoeck, E. F., et al. 2016, *A&A*, 590, A105

Bica, E., Dutra, C. M., & Barbuy, B. 2003, *A&A*, 397, 177

Bressan, A., Marigo, P., Girardi, L., et al. 2012, *MNRAS*, 427, 127

Bronfman, L., Nyman, L. A., & May, J. 1996, *A&AS*, 115, 81

Bruderer, S., Benz, A. O., Doty, S. D., van Dishoeck, E. F., & Bourke, T. L. 2009, *ApJ*, 700, 872

Butner, H. M., Evans, Neal J., I., Harvey, P. M., et al. 1990, *ApJ*, 364, 164

Chen, Y., Bressan, A., Girardi, L., et al. 2015, *MNRAS*, 452, 1068

Chen, Y., Girardi, L., Bressan, A., et al. 2014, *MNRAS*, 444, 2525

Cyganowski, C. J., Brogan, C. L., Hunter, T. R., Churchwell, E., & Zhang, Q. 2011, *ApJ*, 729, 124

Cyganowski, C. J., Whitney, B. A., Holden, E., et al. 2008, *AJ*, 136, 2391

Dunham, M. M., Allen, L. E., Evans, Neal J., I., et al. 2015, *ApJS*, 220, 11

Elia, D., Merello, M., Molinari, S., et al. 2021, *MNRAS*, 504, 2742

Elia, D., Molinari, S., Fukui, Y., et al. 2013, *ApJ*, 772, 45

Elitzur, M., Hollenbach, D. J., & McKee, C. F. 1989, *ApJ*, 346, 983

Esteban, C., & García-Rojas, J. 2018, *MNRAS*, 478, 2315

Faúndez, S., Bronfman, L., Garay, G., et al. 2004, *A&A*, 426, 97

Fernández-Martín, A., Pérez-Montero, E., Vílchez, J. M., & Mampaso, A. 2017, *A&A*, 597, A84

Fischer, C., Beckmann, S., Bryant, A., et al. 2018, *Journal of Astronomical Instrumentation*, 7, 1840003

Fischer, C., Iserlohe, C., Vacca, W., et al. 2021, *PASP*, 133, 055001

Flower, D. R. & Pineau des Forêts, G. 2012, *MNRAS*, 421, 2786

Frank, A., Ray, T. P., Cabrit, S., et al. 2014, in *Protostars and Planets VI*, ed. H. Beuther, R. S. Klessen, C. P. Dullemond, & T. Henning, 451

Furuya, R. S., Kitamura, Y., Wootten, A., Claussen, M. J., & Kawabe, R. 2003a, *ApJS*, 144, 71

Furuya, R. S., Kitamura, Y., Wootten, A., Claussen, M. J., & Kawabe, R. 2003b, *ApJS*, 144, 71

Giannini, T., Massi, F., Podio, L., et al. 2005, *A&A*, 433, 941

Goicoechea, J. R., Cernicharo, J., Karska, A., et al. 2012, *A&A*, 548, A77

Goldsmith, P. F. & Langer, W. D. 1978, *ApJ*, 222, 881

Goldsmith, P. F. & Langer, W. D. 1999, *ApJ*, 517, 209

Graczyk, D., Pietrzyński, G., Thompson, I. B., et al. 2014, *ApJ*, 780, 59

Green, J. D., Evans, Neal J., I., Jørgensen, J. K., et al. 2013, *ApJ*, 770, 123

Green, J. D., Yang, Y.-L., Evans, Neal J., I., et al. 2016, *AJ*, 151, 75

Griffin, M. J., Abergel, A., Abreu, A., et al. 2010, *A&A*, 518, L3

Guevara, C., Stutzki, J., Ossenkopf-Okada, V., et al. 2020, *A&A*, 636, A16

Gyulbudaghian, A. L. 2012, *Astrophysics*, 55, 92

Habing, H. J. 1968, *Bull. Astron. Inst. Netherlands*, 19, 421

Hachisuka, K., Brunthaler, A., Menten, K. M., et al. 2006, *ApJ*, 645, 337

Hatchell, J. & van der Tak, F. F. S. 2003, *A&A*, 409, 589

He, J. H., Takahashi, S., & Chen, X. 2012, *ApJS*, 202, 1

Herczeg, G. J., Karska, A., Bruderer, S., et al. 2012, *A&A*, 540, A84

Heyer, M. & Dame, T. M. 2015, *ARA&A*, 53, 583

Hollenbach, D. & McKee, C. F. 1989, *ApJ*, 342, 306

Hollenbach, D. J. & Tielens, A. G. G. M. 1997, *ARA&A*, 35, 179

Inmer, K., Reid, M. J., Menten, K. M., Brunthaler, A., & Dame, T. M. 2013, *A&A*, 553, A117

Iserlohe, C., Fischer, C., Vacca, W. D., et al. 2021, *PASP*, 133, 055002

Jakob, H., Kramer, C., Simon, R., et al. 2007, *A&A*, 461, 999

Jiménez-Donaire, M. J., Meeus, G., Karska, A., et al. 2017, *A&A*, 605, A62

Johnstone, D., Fich, M., McCoey, C., et al. 2010, *A&A*, 521, L41

Karska, A., Herczeg, G. J., van Dishoeck, E. F., et al. 2013, *A&A*, 552, A141

Karska, A., Herpin, F., Bruderer, S., et al. 2014a, *A&A*, 562, A45

Karska, A., Kaufman, M. J., Kristensen, L. E., et al. 2018, *ApJS*, 235, 30

Karska, A., Koprowski, M., Solarz, A., et al. 2022, *arXiv e-prints*, arXiv:2204.11687

Karska, A., Kristensen, L. E., van Dishoeck, E. F., et al. 2014b, *A&A*, 572, A9

Kaufman, M. J. & Neufeld, D. A. 1996a, *ApJ*, 456, 611

Kaufman, M. J. & Neufeld, D. A. 1996b, *ApJ*, 456, 611

Kaufman, M. J., Wolfire, M. G., & Hollenbach, D. J. 2006, *ApJ*, 644, 283

Klein, R., Beckmann, S., Bryant, A., et al. 2014, in *Society of Photo-Optical Instrumentation Engineers (SPIE) Conference Series*, Vol. 9147, *Ground-based and Airborne Instrumentation for Astronomy V*, ed. S. K. Ramsay, I. S. McLean, & H. Takami, 91472X

Kristensen, L. E., Gusdorf, A., Mottram, J. C., et al. 2017a, *A&A*, 601, L4

Kristensen, L. E., van Dishoeck, E. F., Bergin, E. A., et al. 2012, *A&A*, 542, A8

Kristensen, L. E., van Dishoeck, E. F., Mottram, J. C., et al. 2017b, *A&A*, 605, A93

Kuchar, T. A. & Bania, T. M. 1994, *ApJ*, 436, 117

Ladd, E. F., Deane, J. R., Sanders, D. B., & Wynn-Williams, C. G. 1993, *ApJ*, 419, 186

Ladyschikov, D. A., Gong, Y., Sobolev, A. M., et al. 2022, *ApJS*, 261, 14

Laurini, S., Wyrowski, F., Wiesemeyer, H., et al. 2015, *A&A*, 584, A70

Lew, B. 2018, *Experimental Astronomy*, 45, 81

Liseau, R., Lorenzetti, D., Nisini, B., Spinoglio, L., & Moneti, A. 1992, *A&A*, 265, 577

Litvak, M. M. 1969, *Science*, 165, 855

Lombardi, M., Alves, J., & Lada, C. J. 2011, *A&A*, 535, A16

Manoj, P., Watson, D. M., Neufeld, D. A., et al. 2013, *ApJ*, 763, 83

Marsh, K. A., Whitworth, A. P., Lomax, O., et al. 2017, *MNRAS*, 471, 2730

Matuszak, M., Karska, A., Kristensen, L. E., et al. 2015, *A&A*, 578, A20

Melnick, G. J. & Kaufman, M. J. 2015, *ApJ*, 806, 227

Menten, K. M., Reid, M. J., Pratap, P., Moran, J. M., & Wilson, T. L. 1992, *ApJ*, 401, L39

Minier, V., André, P., Bergman, P., et al. 2009, *A&A*, 501, L1

Mirocha, A., Karska, A., Gronowski, M., et al. 2021, *A&A*, 656, A146

Molinari, S., Swinyard, B., Bally, J., et al. 2010, *A&A*, 518, L100

Mookerjee, B., Sandell, G., Veena, V. S., et al. 2021, *A&A*, 648, A40

Moscadelli, L., Reid, M. J., Menten, K. M., et al. 2009, *ApJ*, 693, 406

Motogi, K., Sorai, K., Habe, A., et al. 2011, *PASJ*, 63, 31

Mottram, J. C., van Dishoeck, E. F., Kristensen, L. E., et al. 2017, *A&A*, 600, A99

Navarete, F., Damineli, A., Barbosa, C. L., & Blum, R. D. 2015, *MNRAS*, 450, 4364

Neckel, T. 1978, *A&A*, 69, 51

Nisini, B., Santangelo, G., Giannini, T., et al. 2015, *ApJ*, 801, 121

Oliveira, J. M., van Loon, J. T., Sewilo, M., et al. 2019, *MNRAS*, 490, 3909

Ossenkopf, V., Röllig, M., Simon, R., et al. 2010, *A&A*, 518, L79

Pickett, H. M., Poynter, R. L., Cohen, E. A., et al. 1998, *J. Quant. Spectr. Rad. Transf.*, 60, 883

Pietrzyński, G., Graczyk, D., Gieren, W., et al. 2013, *Nature*, 495, 76

Pilbratt, G. L., Riedinger, J. R., Passvogel, T., et al. 2010, *A&A*, 518, L1

Poglitsch, A., Waelkens, C., Geis, N., et al. 2010, *A&A*, 518, L2



- Pound, M. W. & Wolfire, M. G. 2011, PDRT: Photo Dissociation Region Toolbox
- Purser, S. J. D., Lumsden, S. L., Hoare, M. G., & Kurtz, S. 2021, MNRAS, 504, 338
- Risacher, C., Güsten, R., Stutzki, J., et al. 2018, Journal of Astronomical Instrumentation, 7, 1840014
- Robitaille, T. P. 2017, A&A, 600, A11
- Robitaille, T. P., Whitney, B. A., Indebetouw, R., & Wood, K. 2007, ApJS, 169, 328
- Roman-Duval, J., Jackson, J. M., Heyer, M., Rathborne, J., & Simon, R. 2010, ApJ, 723, 492
- Russell, S. C. & Dopita, M. A. 1992, ApJ, 384, 508
- Rygl, K. L. J., Brunthaler, A., Sanna, A., et al. 2012, A&A, 539, A79
- Sandell, G. 2000, A&A, 358, 242
- Sandell, G. & Sievers, A. 2004, ApJ, 600, 269
- Schöier, F. L., van der Tak, F. F. S., van Dishoeck, E. F., & Black, J. H. 2005, A&A, 432, 369
- Sewilo, M., Whitney, B. A., Yung, B. H. K., et al. 2019, ApJS, 240, 26
- Shevchenko, V. S. & Yakubov, S. D. 1989, Soviet Ast., 33, 370
- Soares, J. B. & Bica, E. 2002, A&A, 388, 172
- Soares, J. B. & Bica, E. 2003, A&A, 404, 217
- Sodroski, T. J., Odegard, N., Arendt, R. G., et al. 1997, ApJ, 480, 173
- Stanke, T., McCaughrean, M. J., & Zinnecker, H. 2000, A&A, 355, 639
- Szymczak, M., Hrynek, G., & Kus, A. J. 2000, A&AS, 143, 269
- Szymczak, M., Olech, M., Wolak, P., Bartkiewicz, A., & Gawroński, M. 2016, MNRAS, 459, L56
- Tang, J., Bressan, A., Rosenfield, P., et al. 2014, MNRAS, 445, 4287
- Tapia, M., Persi, P., Bohigas, J., & Ferrari-Toniolo, M. 1997, AJ, 113, 1769
- Tobin, J. J., Stutz, A. M., Manoj, P., et al. 2016, ApJ, 831, 36
- Urquhart, J. S., Hoare, M. G., Lumsden, S. L., et al. 2012, MNRAS, 420, 1656
- Urquhart, J. S., Morgan, L. K., Figura, C. C., et al. 2011, MNRAS, 418, 1689
- Vacca, W., Clarke, M., Perera, D., Fadda, D., & Holt, J. 2020, in Astronomical Society of the Pacific Conference Series, Vol. 527, Astronomical Data Analysis Software and Systems XXIX, ed. R. Pizzo, E. R. Deul, J. D. Mol. J. de Plaa, & H. Verkouter, 547
- Valdettaro, R., Palla, F., Brand, J., et al. 2001, A&A, 368, 845
- van der Tak, F. F. S. 2012, Philosophical Transactions of the Royal Society of London Series A, 370, 5186
- van der Tak, F. F. S., van Dishoeck, E. F., Evans, Neal J., I., Bakker, E. J., & Blake, G. A. 1999, ApJ, 522, 991
- van Dishoeck, E. F., Kristensen, L. E., Benz, A. O., et al. 2011, PASP, 123, 138
- van Dishoeck, E. F., Kristensen, L. E., Mottram, J. C., et al. 2021, A&A, 648, A24
- Visser, R., Kristensen, L. E., Bruderer, S., et al. 2012, A&A, 537, A55
- White, G. J., Abergel, A., Spencer, L., et al. 2010, A&A, 518, L114
- Wiesenfeld, L. & Goldsmith, P. F. 2014, ApJ, 780, 183
- Wilson, B. A., Dame, T. M., Masheder, M. R. W., & Thaddeus, P. 2005, A&A, 430, 523
- Wood, D. O. S. & Churchwell, E. 1989, ApJ, 340, 265
- Wouterloot, J. G. A. & Brand, J. 1989, A&AS, 80, 149
- Xu, Y., Reid, M. J., Menten, K. M., et al. 2009, ApJ, 693, 413
- Yang, Y.-L., Evans, N. J., Karska, A., et al. 2022a, ApJ, 925, 93
- Yang, Y.-L., Green, J. D., Evans, Neal J., I., et al. 2018, ApJ, 860, 174
- Yang, Y.-L., Green, J. D., Pontoppidan, K. M., et al. 2022b, ApJ, 941, L13

## Appendix A: Water masers in CMa–I224

### Appendix A.1: Survey results

Water masers are important signposts of both low- and high-mass star formation; they are collisionally excited, tracing warm molecular gas behind shock waves in the environment of YSOs and H II regions (e.g., Litvak 1969; Elitzur et al. 1989; Furuya et al. 2003b; Ladeyschikov et al. 2022 and references therein). Figure A.1 shows the pointings of our 22 GHz water maser survey of the CMa–I224 star-forming region with the 32-m radio telescope in Toruń (RT4; a half-power beam width, HPBW $\sim$ 106'', corresponding to  $\sim$ 0.5 pc at 1 kpc; see Section 2.3), overlaid on the CO 1–0 integrated intensity image from the Forgotten Quadrant Survey (FQS, Benedettini et al. 2020; HPBW $\sim$ 55'' at 115 GHz). The RT4 water maser survey targeted the fields harboring YSO candidates identified by Sewiło et al. (2019). Out of 205 observed fields, (185, 18, 2) were observed in (2, 3, 6) epochs. Water masers were detected toward two fields, one centered on Gy 3–7 and the other on source IRAS 07069–1026 in the main filament in CMa–I224. The very low detection rate is likely the result of the low sensitivity of our observations and the variability of the maser emission (see Section 2.3).

The detection of the water maser toward IRAS 07069–1026 constitutes the first maser detection toward this source, while the detection toward Gy 3–7 has previously been reported in the literature. Urquhart et al. (2011) detected the 22 GHz water maser emission toward Gy 3–7 (their source G224.6075–01.0063) with the 100-m Green Bank Telescope (GBT; HPBW $\sim$ 30''). Water masers were detected toward two other locations in CMa–I224 by Valdetarro et al. (2001) with the Medicina 32-m radio telescope (a similar angular resolution as for RT4), toward IRAS 07077–1026 and IRAS 07054–1039 (see Figure A.1).

The water maser spectra for Gy 3–7 and IRAS 07069–1026 for all epochs of the RT4 observations are shown in Figure A.2

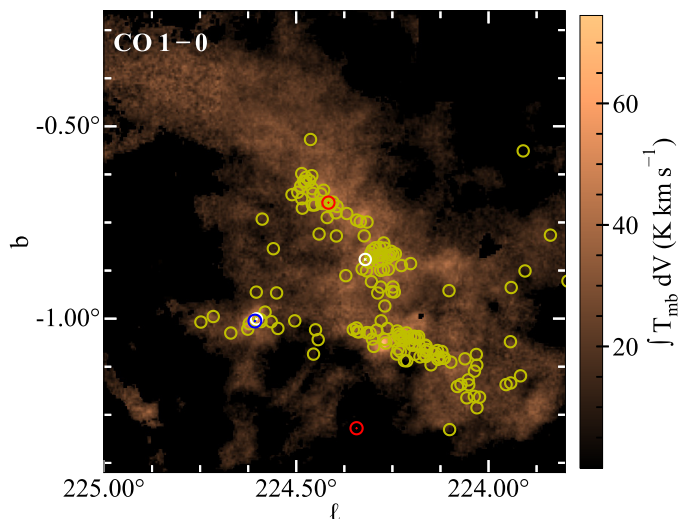


Fig. A.1: CO 1 – 0 integrated intensity map of CMa–I224. Yellow circles show all RT4 pointings, while white circles indicate those with the 22 GHz water maser detections: toward Gy 3–7 and source IRAS 07069–1026 in the main filament. Blue and red circles indicate the positions of water masers detected toward CMa–I224 with the GBT (Urquhart et al. 2011) and the Medicina telescope (Valdetarro et al. 2001), respectively (see text for details).

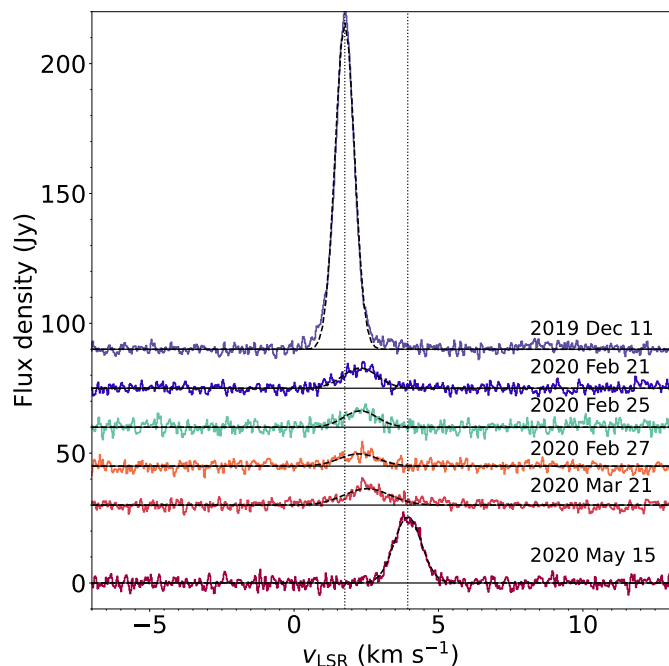


Fig. A.2: 22 GHz H<sub>2</sub>O maser spectra obtained toward Gy 3–7 with the 32-m radio telescope in Toruń from December 2019 to May 2020. The date of observations is indicated above each spectrum. Except for the spectrum corresponding to the observation on May 15, 2020, spectra are shifted vertically by 30 Jy (for the observation on March 21, 2020) and 15 Jy (for the remaining observations) to improve the clarity of the figure. Dashed vertical lines show central velocities of the lines detected in the latest (May 15, 2020) and earliest (December 11, 2019) of the six epochs of observations (see also Table A.1).

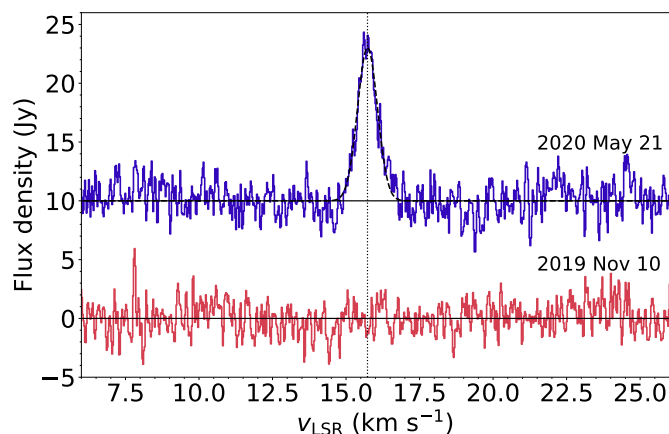


Fig. A.3: 22 GHz H<sub>2</sub>O maser emission detected toward IRAS 07069–1026 (see also Table A.1). The H<sub>2</sub>O maser was detected only in one of the two observing epochs. The spectrum observed on May 21, 2020 is shifted vertically by 10 Jy to improve the clarity of the figure.

and Figure A.3, respectively. Gy 3–7 was observed with RT4 six times over five months with the time interval between subsequent epochs ranging from 2 days to over two months (see Table A.1 for observing dates). The water maser emission was detected in all epochs. IRAS 07069–1026 was observed in two epochs separated by about six months (see Table A.1). The wa-

Table A.1: Parameters of the 22 GHz H<sub>2</sub>O maser lines detected toward CMa–1224 with RT4

Obs. date	$V_p$ (km s <sup>-1</sup> )	$S_p$ (Jy)	FWHM (km s <sup>-1</sup> )	$\int S dV$ (Jy km s <sup>-1</sup> )
Gy 3–7				
2019 Dec 11	1.76 ± 0.01	117.33 ± 0.43	0.79 ± 0.003	41.65 ± 0.32
2020 Feb 21	2.28 ± 0.03	7.27 ± 0.25	1.42 ± 0.06	4.67 ± 0.33
2020 Feb 25	2.30 ± 0.04	5.87 ± 0.35	1.36 ± 0.09	3.61 ± 0.45
2020 Feb 27	2.23 ± 0.08	4.41 ± 0.43	1.59 ± 0.18	3.16 ± 0.66
2020 Mar 21	2.53 ± 0.06	5.87 ± 0.33	1.90 ± 0.12	5.04 ± 0.60
2020 May 15	3.94 ± 0.01	23.80 ± 0.33	1.11 ± 0.02	11.93 ± 0.35
IRAS 07069–1026				
2020 May 21	15.73 ± 0.02	12.15 ± 0.40	0.80 ± 0.03	4.38 ± 0.31

ter maser emission toward IRAS 07069–1026 was only detected in the second epoch, illustrating a high variability of the water maser phenomenon. The RT4 spectra of Gy 3–7 also show clear evidence for a variable nature of the maser emission in this region. Both the peak flux density and central velocity of the maser spots varied significantly between April 2019 and May 2020, covering the flux density and velocity ranges of 4.4–117.2 Jy and 1.8–3.9 km s<sup>-1</sup>, respectively.

The Gauss functions were fitted to the 22 GHz water maser lines observed towards Gy 3–7 and IRAS 07069–1026. The Gauss fitting results are shown Table A.1: the central velocities ( $V_p$ ) of the water maser lines, their peak flux densities ( $S_p$ ), full-widths at half maximum (FWHM), and the integrated flux densities ( $\int S dV$ ). The measured flux densities are likely underestimated by 10–20% due to the atmospheric conditions at the observatory site; no correction for atmospheric attenuation was applied.

#### Appendix A.2: Water maser emission in Gy 3–7

Urquhart et al. (2011) report the detection of a single water maser spot toward Gy 3–7 (G224.6075–01.0063) with the peak flux density of 2.57 Jy and velocity of 28.7 km s<sup>-1</sup> (~25 km s<sup>-1</sup> higher than the emission detected with RT4). However, the inspection of the spectrum provided by Urquhart et al. (2011) reveals a second, much fainter and broader water maser line centered at the velocity of ~0 km s<sup>-1</sup>, only ~2–4 km s<sup>-1</sup> lower than the peak velocities of the lines detected in our observations. No water maser emission at higher velocities was detected in any of the six RT4 epochs.

The systemic velocity of Gy 3–7 is 16.7 km s<sup>-1</sup> based on the NH<sub>3</sub> observations of Urquhart et al. (2011), in a very good agreement with the CO 1–0 velocity of ~16 km s<sup>-1</sup> (Benedettini et al. 2020), indicating that NH<sub>3</sub> and CO trace the same molecular gas. The water maser emission toward Gy 3–7 is blueshifted (this study) and redshifted (Urquhart et al. 2011) with respect to the systemic velocity. The blueshifted emission has the similar velocity offset (~13–16 km s<sup>-1</sup>) from the systemic velocity as the redshifted emission (12 km s<sup>-1</sup>), extending the velocity range over which the maser spots are found toward Gy 3–7 from ~2 km s<sup>-1</sup> reported in Urquhart et al. (2011) to ~30 km s<sup>-1</sup>.

About 60% of the sources from the Urquhart et al. (2011) sample have total velocity ranges of the water maser emission of  $\lesssim 20$  km s<sup>-1</sup>. The mean/median velocity range of the entire sample is 24.7/15.2 km s<sup>-1</sup>. Six sources have velocity ranges of >100 km s<sup>-1</sup>. The Gy 3–7's water maser velocity range of ~30 km s<sup>-1</sup> is larger than the velocity ranges of the majority of

the sources from the Urquhart et al. (2011) sample, but it is well within the observed values.

The water maser data currently available for Gy 3–7 show that the blueshifted water maser spots are brighter than the redshifted ones (and thus detected more often), in agreement with the results obtained by Urquhart et al. (2011) for a large sample of ~300 YSOs and H II regions. The higher relative velocities of blueshifted masers also agree with the Urquhart et al. (2011)' results.

The difference of ~12–16 km s<sup>-1</sup> between the systemic velocity of Gy 3–7 and the velocities of maser spots is small enough to assume that there is the physical association between the molecular gas traced by NH<sub>3</sub> and CO and the maser emission (possibly originating in outflow shocks); it is less likely that the maser emission is arising from a different region located along the same line of sight. The mean difference between the maser and systemic velocities for the Urquhart et al. (2011) sample of YSOs and H II regions is -3.8 km s<sup>-1</sup>, but with the large standard deviation (~20 km s<sup>-1</sup>). It is possible that the water maser emission with smaller offsets from the systemic velocity of Gy 3–7 exists, but remained undetected due to the maser variability and/or limited sensitivity of the observations.

The spatial resolution of the existing water maser observations of Gy 3–7 is too low to accurately pinpoint the location of the maser spots in the region. Higher resolution observations are needed to investigate the distribution of the maser spots toward Gy 3–7 and the origin of the maser emission. Systematic monitoring of the water maser activity at high angular resolution would be necessary to constrain any periodicity in the maser line intensity in one or more velocity components (Szymczak et al. 2016).

## Appendix B: Spatial extent of FIR line emission

Figures B.1 and B.2 show the spatial extent of the [O I] lines at 63 and 145  $\mu$ m, the [C II] line at 157  $\mu$ m, the CO lines with  $J_{\text{up}} = 14 - 31$ , and the OH line at 79.2  $\mu$ m. We calculated the flux of these emission line toward the two dense cores A and B, within a beam size of 20'' (Table B.1). Since all lines are spectrally-unresolved, the line fluxes are obtained using Gaussian fits and their uncertainties are estimated as  $1\sigma$  of the distribution of 10 000 Gaussian profiles generated based on the parameters of the Gaussian fit and their uncertainty.

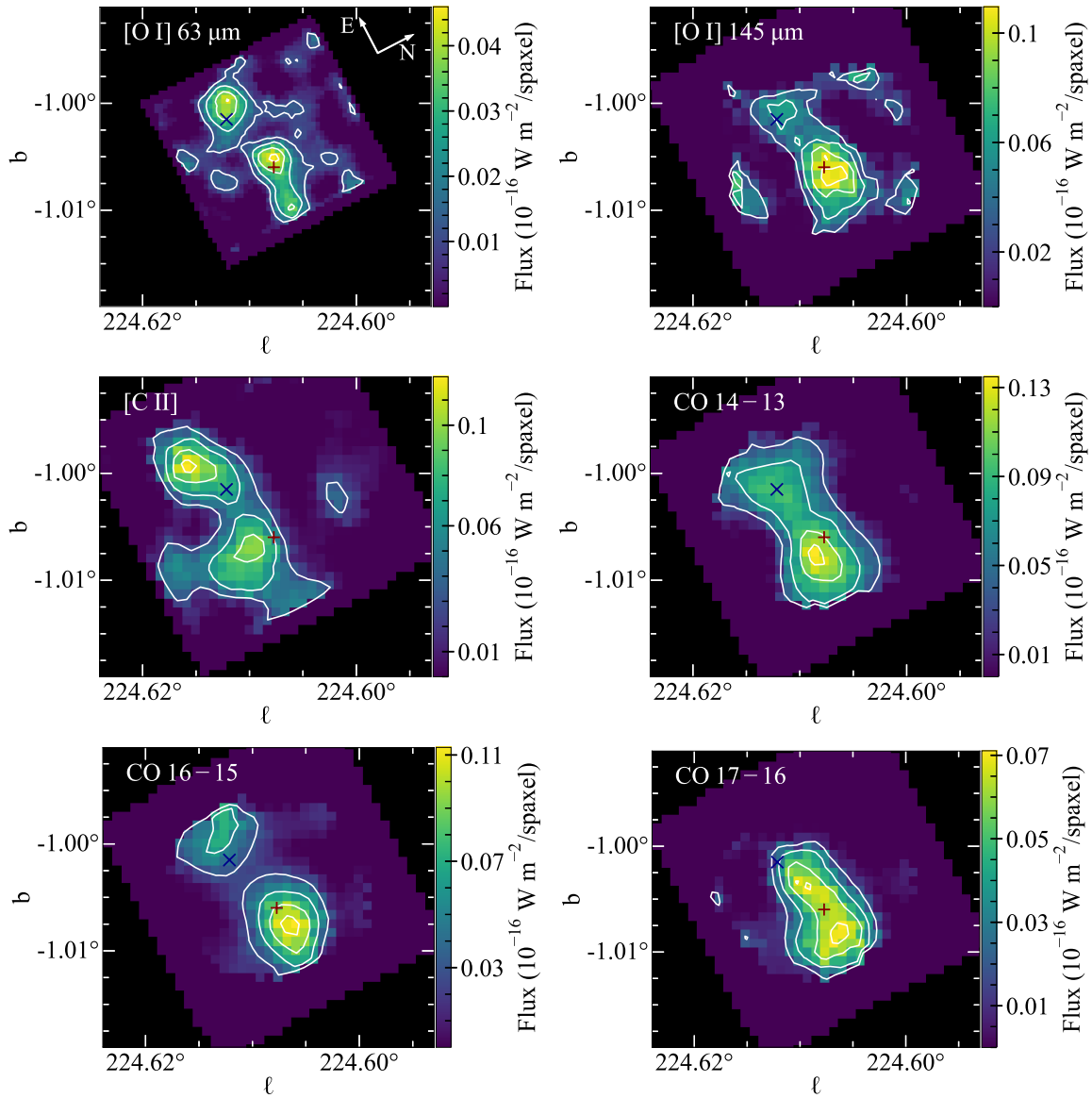


Fig. B.1: FIFI-LS integrated intensity maps of the [O I] lines at 63.2 and 145.5  $\mu\text{m}$ , the [C II] line at 157.7  $\mu\text{m}$ , the CO lines  $J = 14 - 13$ ,  $16 - 15$ ,  $17 - 16$  at 186, 162.8, 153.3  $\mu\text{m}$ , respectively. The white contours show line emission at 25%, 50%, 75%, and 95% of the corresponding line emission peak. The "+" and "x" signs show the positions of the dense cores A and B, respectively.

Table B.1: Flux SOFIA FIFI-LS toward the two dense cores within a beam size of  $20''$ .

$\lambda$ ( $\mu\text{m}$ )	Flux ( $10^{-16} \text{ W m}^{-2}$ )	
	core A	core B
63.18	$29.65 \pm 1.60$	$24.37 \pm 1.72$
84.41	$4.93 \pm 1.80$	–
87.19	$1.81 \pm 0.53$	–
118.58	$2.68 \pm 0.21$	–
157.74	$1.15 \pm 0.07$	$1.90 \pm 0.09$
145.53	$2.68 \pm 0.09$	$1.97 \pm 0.12$
153.27	$2.09 \pm 0.05$	$1.09 \pm 0.07$
162.81	$2.84 \pm 0.05$	$1.80 \pm 0.07$
186.00	$2.73 \pm 0.08$	$2.56 \pm 0.13$

## Appendix C: Multi-wavelength photometry and SED fitting results

Table C.1 shows the multi-wavelength photometry for 15 YSO candidates in Gy 3–7. Figure C.1 shows the SEDs of YSO candidates in Gy 3–7 with the best-fit Robitaille (2017) models. Figure C.2 shows the Hertzsprung-Russell diagram with the positions of the YSOs obtained from the SED modeling in line with the PMS tracks.

We note that sources numbered 3 – 8 and source 11 lack continuum measurements at  $> 4.5 \mu\text{m}$ , which limits the SED modeling. The best-fit models for sources No. 4 – 6 and 11 are stars (Table 4), since the envelope emission could not be traced. Near-IR observations show some IR excess toward source No. 6 (Tapia et al. 1997), but the confirmation of its YSO status would require additional observations, which are outside of the scope of this paper.



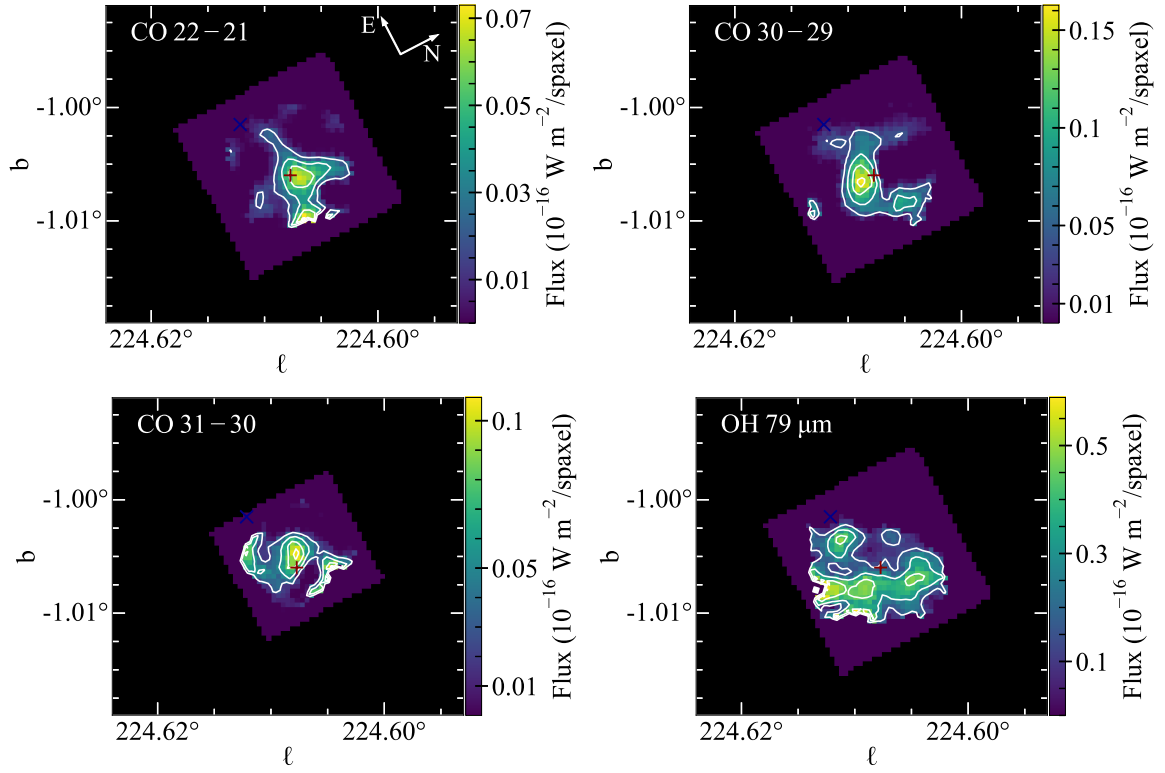


Fig. B.2: FIFI-LS integrated intensity maps of the CO 22 – 21, CO 30 – 29 , and CO 31 – 30 transitions at 118, 84, and 87  $\mu\text{m}$ , respectively, and the OH line at 79.2  $\mu\text{m}$ . The white contours show line emission at 25%, 50%, 75%, and 95% of the corresponding line emission peak, see also Figure B.1.

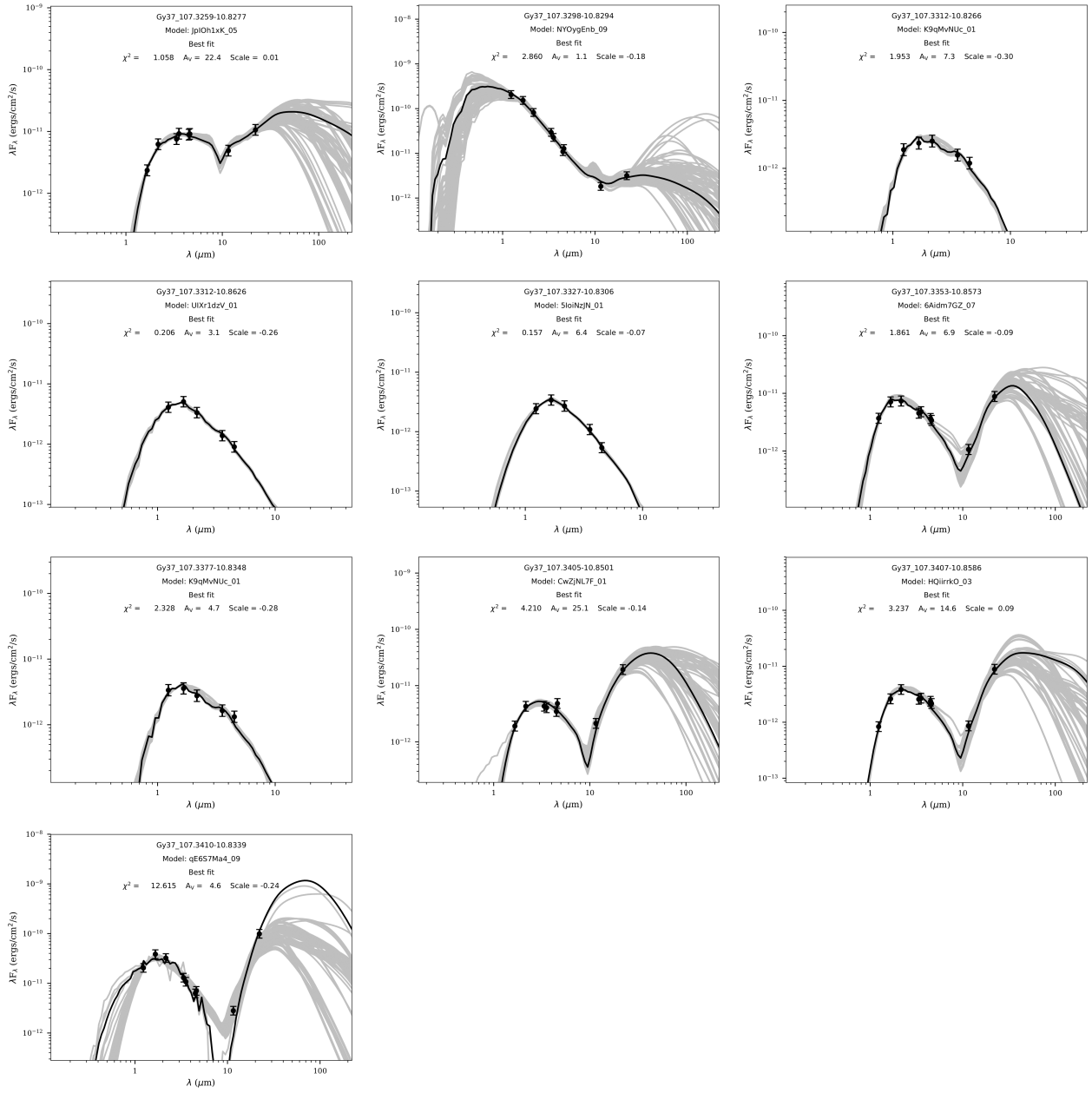


Fig. C.1: SEDs of YSO candidates with well-fitted Robitaille (2017) YSO models. The best-fit model is indicated with the black solid line. Gray lines show the YSO models with  $\chi^2$  between  $\chi^2_{\text{best}}$  and  $\chi^2_{\text{best}} + F \times n$ , where  $n$  is the number of data points and  $F$  is a threshold parameter which we set to 3 (Sewilo et al. 2019). Filled circles and triangles are valid flux values and flux upper limits, respectively. The values of a reduced  $\chi^2$  and interstellar visual extinction for the best-fit model are indicated in the plots.

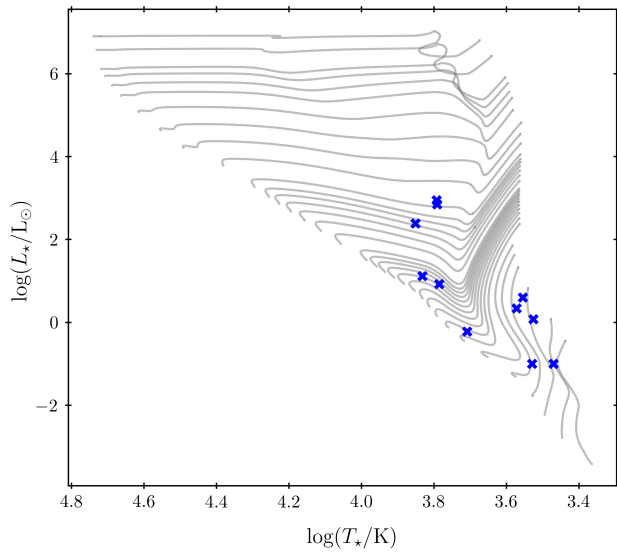


Fig. C.2: HR diagram with YSOs in Gy 3–7 (blue ‘x’ symbols) and the PARSEC evolutionary tracks (Bressan et al. 2012; Chen et al. 2014, 2015; Tang et al. 2014).

Table C.1: Multi-wavelength photometry of YSO candidates in the IRAS field. The columns represent the 2MASS  $JHK_s$ , *Spitzer* IRAC 3.6 and 4.5  $\mu\text{m}$ , AllWISE, *Herschel* PACS, and SPIRE

ID	RA (deg)	Dec (deg)	$S_J$ (mJy)	$S_H$ (mJy)	$S_K$ (mJy)	$S_{3.6}$ (mJy)	$S_{4.5}$ (mJy)	$S_{W1}$ (mJy)	$S_{W2}$ (mJy)
1	107.32592	-10.82772	...	$1.33 \pm 0.06$	$4.56 \pm 0.13$	$11.11 \pm 0.43$	$13.57 \pm 0.30$	$8.59 \pm 0.18$	$14.28 \pm 0.27$
2	107.32975	-10.82944	$86.55 \pm 2.07$	$86.28 \pm 2.07$	$60.13 \pm 1.27$	$27.44 \pm 1.05$	$16.67 \pm 0.57$	$33.60 \pm 0.72$	$20.02 \pm 0.43$
3	107.33013	-10.83094	...	$2.33 \pm 0.33$	$3.15 \pm 0.26$	$2.61 \pm 0.10$	$2.63 \pm 0.07$	...	...
4	107.33121	-10.82658	$0.79 \pm 0.07$	$1.33 \pm 0.07$	$1.85 \pm 0.12$	$1.89 \pm 0.08$	$1.82 \pm 0.05$	...	...
5	107.33121	-10.86256	$1.72 \pm 0.06$	$2.86 \pm 0.12$	$2.45 \pm 0.13$	$1.67 \pm 0.06$	$1.38 \pm 0.04$	...	...
6	107.33275	-10.83064	$1.02 \pm 0.06$	$1.92 \pm 0.09$	$1.98 \pm 0.12$	$1.31 \pm 0.06$	$0.82 \pm 0.04$	...	...
7	107.33379	-10.84222	$2.33 \pm 0.24$	$14.68 \pm 1.47$	$23.61 \pm 2.36$	...	...	...	...
8	107.33467	-10.84192	$2.59 \pm 0.35$	$16.75 \pm 1.67$	$32.03 \pm 3.20$	...	...	...	...
9	107.33529	-10.85725	$1.55 \pm 0.08$	$4.01 \pm 0.11$	$5.40 \pm 0.19$	$5.79 \pm 0.21$	$5.58 \pm 0.16$	$5.16 \pm 0.12$	$5.31 \pm 0.11$
10	107.33563	-10.84117	$1.17 \pm 0.16$	$4.57 \pm 0.65$	$21.06 \pm 1.46$	...	...	$87.24 \pm 1.79$	$403.08 \pm 7.87$
11	107.33771	-10.83483	$1.41 \pm 0.07$	$2.02 \pm 0.07$	$2.03 \pm 0.10$	$1.98 \pm 0.07$	$2.02 \pm 0.07$	...	...
12	107.33879	-10.84178	$1.47 \pm 0.15$	$1.16 \pm 0.20$	$3.22 \pm 0.30$	...	...	$24.38 \pm 2.28$	$52.26 \pm 1.41$
13	107.34054	-10.85011	...	$1.08 \pm 0.07$	$3.15 \pm 0.10$	$4.89 \pm 0.21$	$5.30 \pm 0.11$	$4.91 \pm 0.10$	$7.53 \pm 0.10$
14	107.34071	-10.85858	$0.35 \pm 0.05$	$1.48 \pm 0.09$	$2.82 \pm 0.13$	$3.25 \pm 0.12$	$3.62 \pm 0.14$	$2.93 \pm 0.06$	$3.38 \pm 0.07$
15	107.34100	-10.83386	$8.58 \pm 0.29$	$21.79 \pm 0.60$	$23.65 \pm 0.50$	$12.97 \pm 0.61$	$9.56 \pm 0.36$	$14.79 \pm 0.27$	$11.00 \pm 0.18$
ID	RA (deg)	Dec (deg)	$S_{W3}$ (mJy)	$S_{W4}$ (mJy)	$S_{70}$ (Jy)	$S_{160}$ (Jy)	$S_{250}$ (Jy)	$S_{350}$ (Jy)	$S_{500}$ (Jy)
1	107.32592	-10.82772	$19.26 \pm 0.41$	$79.72 \pm 2.92$	...	...	...	...	...
2	107.32975	-10.82944	$7.16 \pm 0.28$	$23.74 \pm 1.56$	...	...	...	...	...
3	107.33013	-10.83094	...	...	...	...	...	...	...
4	107.33121	-10.82658	...	...	...	...	...	...	...
5	107.33121	-10.86256	...	...	...	...	...	...	...
6	107.33275	-10.83064	...	...	...	...	...	...	...
7	107.33379	-10.84222	...	...	...	...	...	...	...
8	107.33467	-10.84192	...	...	...	...	...	...	...
9	107.33529	-10.85725	$4.18 \pm 0.19$	$66.19 \pm 2.99$	...	...	...	...	...
10	107.33563	-10.84117	$4017.01 \pm 33.44$	$28890.97 \pm 160.10$	$165.8 \pm 0.5$	$1030.6 \pm 0.4$	$57.0 \pm 0.5$	$23.5 \pm 0.1$	$10.6 \pm 0.1$
11	107.33771	-10.83483	...	...	...	...	...	...	...
12	107.33879	-10.84178	$117.25 \pm 2.62$	$4541.11 \pm 46.24$	$42.5 \pm 0.2$	$60.8 \pm 0.2$	$62.0 \pm 0.6$	$20.8 \pm 0.1$	...
13	107.34054	-10.85011	$8.38 \pm 0.17$	$144.66 \pm 1.34$	...	...	...	...	...
14	107.34071	-10.85858	$3.38 \pm 0.20$	$66.43 \pm 2.62$	...	...	...	...	...
15	107.34100	-10.83386	$11.04 \pm 0.14$	$743.98 \pm 1.37$	...	...	...	...	...



Table D.1: CO rotational temperature and number of emitting molecules for HM YSOs, derived by fitting the rotational diagram of CO using all and only four available CO transitions.

Source	$T_{\text{rot},4}^a$ (K)	$T_{\text{rot},\text{all}}^b$ (K)	$T_{\text{rot}}$ Diff. <sup>c</sup> (%)
G327-0.6	275 ± 60	265 ± 30	4
W51N-e1	270 ± 15	260 ± 15	4
DR21OH	225 ± 25	235 ± 15	4
W33A	135 ± 5	185 ± 25	27
G34.26+0.15	330 ± 60	320 ± 25	3
NGC6334-I	320 ± 55	300 ± 25	7
NGC7538-I1	175 ± 25	185 ± 15	5
AFGL2591	175 ± 10	195 ± 15	10
W3IRS5	335 ± 40	320 ± 15	5
G5.89-0.39	345 ± 40	285 ± 15	21

**Notes.** <sup>(a)</sup> Rotational temperatures calculated using 4 CO transitions with  $J_{\text{up}} = (14, 16, 17, 22)$ . <sup>(b)</sup> Rotational temperatures calculated using all detected CO transitions, data is adopted from [Karska et al. \(2014a\)](#). <sup>(c)</sup> The relative difference of  $T_{\text{rot}}$  is taken as  $|1 - T_{\text{rot},4}/T_{\text{rot},\text{all}}| \times 100$ .

## Appendix D: CO rotational temperature of the intermediate-to high-mass YSOs in the Milky Way

We compare the rotational temperatures towards the two dense cores to the results found in the samples of the IM and HM YSOs in the Milky Way. There are six IM and ten HM YSOs presented in [Karska et al. \(2014a\)](#) and [Matuszak et al. \(2015\)](#), respectively using the data from *Herschel*/PACS. To be consistent with our SOFIA/FIFI-LS data, we recalculated the rotational temperatures derived by fitting the rotational diagram using 4 CO transitions with  $J_{\text{up}} = (14, 16, 18, 22)$  and  $(14, 16, 17, 22)$  for the IM and HM YSOs, respectively.

We checked the new results with the ones presented in the aforementioned studies and find that using only four CO transitions returns a lower  $T_{\text{rot}}$  than the case of using all the observable CO transitions. The relative difference is in between 4-27% with a median of 5% for the HM YSOs. The comparison of these differences is shown in Table D.1.

Table D.2 shows heliocentric distances, Galactocentric radii, metallicities, and luminosities of the sources in the Milky Way and Magellanic Clouds. We used heliocentric distances together with source coordinates to calculate Galactocentric radii, assuming a distance from the Sun to the Galactic center of 8.34 kpc. We estimated the metallicity toward the Milky Way sources using the O/H galactocentric radial gradient based on H II regions in the Galactic disk ([Balsler et al. 2011](#)).

Table D.2: FIR line cooling luminosity of the sample in the Milky Way (MW), LMC, and SMC used to compare with results of this study

Source	$D$ (kpc)	$D$ Ref.	$R_{GC}^a$ (kpc)	$Z^b$ ( $Z_{\odot}$ )	$\log(L_{bol}/L_{\odot})$	$L_{bol}$ Ref.	$L_{CO}^c$ ( $10^{-2}L_{\odot}$ )	$L_{[O I]}^d$ ( $10^{-2}L_{\odot}$ )	$L_{CO}/L_{[O I]}$	$L_{lines}$ Ref.
LMC YSOs										
IRAS04514–6931	$50.0 \pm 1.1$	1	—	0.4	4.8	16	5.3	8.8	0.605	16
N113 YSO3	$50.0 \pm 1.1$	1	—	0.4	5.4	16	29.5	57.8	0.511	16
SAGE045400.9–691151.6	$50.0 \pm 1.1$	1	—	0.4	5.1	16	14.6	29.2	0.5	16
SAGE051351.5–672721.9	$50.0 \pm 1.1$	1	—	0.4	5.1	16	5.5	15.4	0.357	16
SAGE052202.7–674702.1	$50.0 \pm 1.1$	1	—	0.4	4.5	16	4.3	9.4	0.459	16
SAGE052212.6–675832.4	$50.0 \pm 1.1$	1	—	0.4	5.5	16	14.9	25.4	0.585	16
SAGE053054.2–683428.3	$50.0 \pm 1.1$	1	—	0.4	4.9	16	6.8	5.4	1.24	16
ST01	$50.0 \pm 1.1$	1	—	0.4	4.6	16	7.1	8.5	0.833	16
N113 YSO1	$50.0 \pm 1.1$	1	—	0.4	5.4	16	47.5	47.5	1	16
SMC YSOs										
IRAS00464–7322	$62.1 \pm 2.0$	2	—	0.2	4.1	16	3.0	2.8	1.077	16
IRAS00430–7326	$62.1 \pm 2.0$	2	—	0.2	4.9	16	1.9	10.9	0.176	16
N81	$62.1 \pm 2.0$	2	—	0.2	4.7	16	2.4	36.4	0.067	16
SMC012407-730904	$62.1 \pm 2.0$	2	—	0.2	5.3	16	6.8	71.2	0.096	16
MW IM YSOs										
AFGL 490	$0.97 \pm 0.40$	3	9.12	0.7	3.7	17	$24.7 \pm 2.5$	$36.6 \pm 0.2$	$0.7 \pm 0.1$	32
L 1641	$0.428 \pm 0.010$	4	8.69	0.8	1.8	18	$2.7 \pm 0.4$	$1.6 \pm 0.1$	$1.7 \pm 0.3$	32
NGC 2071	$0.422 \pm 0.050$	4	8.71	0.8	2.7	19	$44.8 \pm 4.3$	$33.4 \pm 0.1$	$1.3 \pm 0.1$	32
Vela 17	0.7	5	8.44	0.8	2.9	20	$13.2 \text{ pm } 2.0$	$44.8 \pm 0.1$	$0.3 \pm 0.1$	32
Vela 19	0.7	5	8.45	0.8	2.9	5	$9.7 \pm 2.0$	$14.4 \pm 0.1$	$0.7 \pm 0.1$	32
NGC 7129	1.25	6	8.75	0.8	2.6	21	$20.9 \pm 3.0$	$6.9 \pm 0.1$	$3.0 \pm 0.4$	32
MW HM YSOs										
G327-0.6	3.3	7	5.84	1.0	4.7	22	$180 \pm 60$	$30 \pm 10$	$6.0 \pm 2.8$	33
W51N-e1	$5.1 \pm 2.2$	8	12.42	0.5	5.0	23	$2530 \pm 680$	$760 \pm 180$	$3.3 \pm 1.2$	33
DR21(OH)	$1.50 \pm 0.08$	9	8.26	0.8	4.1	24	$120 \pm 30$	$9 \pm 3$	$13.3 \pm 5.6$	33
W33A	$2.40 \pm 0.16$	10	6.02	1.0	4.6	25	$60 \pm 20$	$5 \pm 2$	$12.0 \pm 6.2$	33
G34.26+0.15	3.30	11	5.91	1.0	5.5	26	$770 \pm 240$	$190 \pm 50$	$4.1 \pm 1.7$	33
NGC6334I	$1.7 \pm 0.3$	12	6.66	0.9	5.4	27	$340 \pm 100$	$4 \pm 3$	$85.0 \pm 68.5$	33
NGC7538-IRS1	$2.7 \pm 0.1$	13	9.66	0.7	5.1	28	$280 \pm 50$	$1100 \pm 250$	$0.2 \pm 0.1$	33
AFGL2591	$3.3 \pm 0.08$	9	8.36	0.9	5.3	29	$160 \pm 50$	$340 \pm 90$	$0.5 \pm 0.2$	33
W3-IRS5	$2.00 \pm 0.07$	14	9.83	0.7	5.2	30	$1050 \pm 250$	$420 \pm 10$	$2.5 \pm 0.8$	33
G5.89-0.39	$1.30 \pm 0.09$	15	7.05	0.9	4.7	31	$390 \pm 90$	$370 \pm 90$	$1.1 \pm 0.4$	33

**References:** (1) Pietrzyński et al. (2013), (2) Graczyk et al. (2014), (3) Purser et al. (2021), (4) Wilson et al. (2005), (5) Liseau et al. (1992), (6) Shevchenko & Yakubov (1989), (7) Minier et al. (2009), (8) Xu et al. (2009), (9) Rygl et al. (2012), (10) Immer et al. (2013), (11) Kuchar & Bania (1994), (12) Neckel (1978), (13) Moscadelli et al. (2009), (14) Hachisuka et al. (2006), (15) Motogi et al. (2011), (16) Oliveira et al. (2019), (17) Navarete et al. (2015), (18) Stanke et al. (2000), (19) Butner et al. (1990), (20) Giannini et al. (2005), (21) Johnstone et al. (2010), (22) Urquhart et al. (2012), (23) van Dishoeck et al. (2011), (24) Jakob et al. (2007), (25) Faúndez et al. (2004), (26) Hatchell & van der Tak (2003), (27) Sandell (2000), (28) Sandell & Sievers (2004), (29) van der Tak et al. (1999), (30) Ladd et al. (1993), (31) van der Tak (2012), (32) Matuszak et al. (2015), (33) Karska et al. (2014a).

<sup>a</sup> Galactocentric radius toward the sources in the Milky Way is calculated using the information from their coordinate and distance to the Sun, assuming the distance from the Sun to the Galactic center is 8.34 kpc.

<sup>b</sup> Metallicity towards the sources in the Milky Way is calculated using the relation of O/H gradients inferred from the H II regions:  $12 + \log(O/H) = -0.0446R_{GC} + 8.962$  (Balsler et al. 2011).

<sup>c</sup> Total FIR luminosity of CO derived from the rotational diagram fitting.

<sup>d</sup> Total FIR luminosity of [O I] calculated by summing the luminosity of [O I] lines at 63 and 145  $\mu\text{m}$ .